The Planetary Science Journal, 7:199 (22pp), 2026 August https://doi.org/10.3847/PSJ/ae8818

Tracing the Source of Carbon Oxides on the Large Moons of Uranus

Richard J. Cartwright[1], Sasha Cryan[2], Rosario Brunetto[2], Apolline Leclef[2], Eric Quirico[3], Bryan J. Holler[4], William M. Grundy[5], Tom A. Nordheim[1], Ujjwal Raut[6], Matthew M. Hedman[7], Riley A. DeColibus[8], Chloe B. Beddingfield[1], Marc Neveu[9,10], Christopher R. Glein[6], Sara Faggi[10,11], Geronimo L. Villanueva[10], Noemi Pinilla-Alonso[12], and Stephanie M. Menten[1]

[1] Johns Hopkins University, Applied Physics Laboratory, 11101, Johns Hopkins Road, Laurel, MD 20723, USA; richard.cartwright@jhuapl.edu
[2] Université Paris-Saclay, CNRS, Institut d'Astrophysique Spatiale, Orsay, France
[3] Université Grenoble Alpes, CNRS, Institut de Planetologie et Astrophysique de Grenoble (IPAG), UMR 5274, Grenoble, F-38041, France
[4] Space Telescope Science Institute, 3700 San Martin Drive, Baltimore, MD 21218, USA
[5] Department of Astronomy and Planetary Science, Northern Arizona University, 527 South Beaver Street, Flagstaff, AZ 86011, USA
[6] Southwest Research Institute, 6220 Culebra Road, San Antonio, TX 78238-5166, USA
[7] Department of Physics, University of Idaho, 875 Perimeter Drive, MS 0903, Moscow, ID 83844-0903, USA
[8] Jet Propulsion Laboratory, California Institute of Technology, 4800 Oak Grove Drive Pasadena, CA 91109, USA
[9] University of Maryland, 4296 Stadium Drive, College Park, MD 20742, USA
[10] Solar System Exploration Division, NASA Goddard Space Flight Center, 8800 Greenbelt Road, Greenbelt, MD 20771, USA
[11] American University, CAS Physics Department, 4400 Massachusetts Avenue NW, Washington, DC 20016, USA
[12] Instituto de Ciencias y Tecnologías Espaciales de Asturias (ICTEA), Oviedo, Asturias, Spain
Received 2026 March 12; revised 2026 June 28; accepted 2026 July 6; published 2026 August 17

Abstract

The Uranian moons Ariel, Umbriel, Titania, and Oberon are enriched in CO_2 mixed with CO, but the origin(s) of these carbon oxides, be they primarily native or radiolytic, remain(s) uncertain. Using data collected by NIRSpec on the James Webb Space Telescope (JWST), we measured the spectral signature of CO_2 and other carbon oxides to help disentangle these hypotheses. Through comparison to laboratory data, we find that many of the detected spectral features are consistent with CO_2 ice, including $^{12}CO_2$ scattering peaks (4.15–4.26 μm), multilobe $^{13}CO_2$ bands (4.35–4.43 μm), and CO_2 biphonon and triphonon modes (4.80–5.25 μm). Our measurements show that CO_2 and CO are concentrated on the trailing hemispheres of the inner moons Ariel and Umbriel, potentially supporting a radiolytic production hypothesis, consistent with prior ground-based results. However, many of the identified spectral features are only observed in thick crystalline ice deposits measured in the laboratory, which may be difficult to form via radiolysis of carbon-bearing material mixed in icy regoliths. Similarly, the data exhibit weak 4.02 and 4.40 μm bands, hinting at the presence of carbonate minerals and $^{13}CO_2$ clathrates, respectively, possibly formed in the interiors of these moons. Furthermore, JWST has revealed that CO_2 is widespread at Uranus, present in its system of rings, ring moons, and irregular satellites, consistent with its largest moons accreting CO_2 and other carbon oxides from the Uranian subnebula. We conclude that exposed carbon oxides are potentially native, with their surface distributions shaped by charged particle irradiation and seasonal sublimation–condensation cycles.

Unified Astronomy Thesaurus concepts: Ice spectroscopy (2250); Surface ices (2117); Carbon dioxide (196); Surface processes (2116); Surface composition (2115); James Webb Space Telescope (2291); Uranian satellites (1750)

1. Introduction

The Voyager 2 (V2) spacecraft made a close pass of the Uranus system in 1986, returning valuable imaging data of its large and tidally locked "classical" Uranian satellites Miranda, Ariel, Umbriel, Titania, and Oberon (B. A. Smith et al. 1986). These data revealed terrains exhibiting a wide range of estimated heat fluxes pointing to periods of intense geologic activity in the past (C. Beddingfield et al. 2015; G. Peterson et al. 2015; C. B. Beddingfield et al. 2022a, 2022b, 2023; M. T. Bland et al. 2023). These images also revealed possible sites of volatile release from within Ariel's interior, including hypothesized cryovolcanic features (P. M. Schenk 1991; C. B. Beddingfield & R. J. Cartwright 2021) and large-scale fissures that could be conduits to its interior, analogous to spreading centers on Earth (C. B. Beddingfield et al. 2025). On Umbriel, a bright annulus in Wunda crater, along with other high-albedo spots (P. Helfenstein et al. 1989) could result from deposits of volatile ices and perhaps internally derived salts (M. M. Sori et al. 2017; R. J. Cartwright et al. 2023; J. E. Scully et al. 2025; C. Denton et al. 2026). However, V2 was not equipped with a near-infrared (NIR) mapping spectrometer and could not deduce the chemical species mantling putative cryovolcanic features and other geologic terrains on the surfaces of Uranus' large moons, nor the species incorporated into its system of rings and ring moons.

In the decades following the V2 flyby, these moons have been regularly observed using ground-based telescopes, primarily at NIR wavelengths (~1–2.5 μm; e.g., W. Grundy et al. 2003; R. J. Cartwright et al. 2023), revealing the presence of weak CO_2 ice features (e.g., W. Grundy et al. 2006; R. J. Cartwright et al. 2015), as well as hints of CO ice (R. J. Cartwright et al. 2022). Analyses conducted by these and other prior studies demonstrated that the distribution of CO_2

exhibits clear spatial trends on the moons, with CO_2 detected primarily on their trailing hemispheres (subobserver longitudes of 181°W–360°W). CO_2 could not be conclusively detected on their leading hemispheres (subobserver longitudes of 1°W–180°W). Furthermore, the inner moons, Ariel and Umbriel, are enriched in CO_2 relative to the outer moons, Titania and Oberon. The spatial trends in the distribution of CO_2 have been cited as evidence for a radiolytic production cycle, whereby charged particles trapped in Uranus' magnetosphere preferentially interact with H_2O ice and carbonaceous material on the trailing hemispheres of the inner moons, forming CO_2 molecules within their regoliths (e.g., O. Gomis & G. Strazzulla 2005; U. Raut et al. 2012). Such a mechanism is perhaps analogous to hypothesized radiolytic production pathways for some of the CO_2 exposed on the surfaces of the icy Galilean satellites (e.g., T. McCord et al. 1997, 1998a; C. Hibbitts et al. 2000).

On the Uranian moons, CO_2 has been identified through the presence of three narrow features centered near 1.966, 2.012, and 2.070 μm, respectively consistent with the $2\nu_1+\nu_3$, $\nu_1+2\nu_2+\nu_3$, and $4\nu_2+\nu_3$ combination and overtone modes measured in "pure" CO_2 ice (i.e., mostly free of impurities), in which CO_2 molecules are presumably organized into a crystalline lattice exhibiting long-range order (e.g., G. B. Hansen 1997; E. Quirico & B. Schmitt 1997a; P. A. Gerakines et al. 2005). This "CO_2 triplet band" has been detected primarily in reflectance spectra collected with the SpeX spectrograph (J. T. Rayner et al. 2003) on NASA's Infrared Telescope Facility (IRTF). More recent ground-based observations suggest that the CO_2 triplet bands are getting progressively weaker as the Uranus system progresses toward northern summer solstice in 2050 (subobserver latitude of 82°N), and the north poles of the moons are gradually exposed to sunlight (R. J. Cartwright et al. 2022). This finding is consistent with volatile migration models that predict long-term cold traps are at low latitudes (30°S–30°N), where diurnal variations in heating dampen sublimation rates relative to the continually sunlit summer poles (W. Grundy et al. 2006; M. M. Sori et al. 2017; J. K. Steckloff et al. 2022; S. M. Menten et al. 2024).

Although ground-based data and results have provided useful information on the spectral properties and distribution of CO_2, the overall weakness of the CO_2 triplet band (band depths of ~1%–15% of the continuum), as well as low levels of residual contamination from telluric CO_2 gas features between 1.9 and 2.1 μm, have constrained prior analyses and limited our understanding of the nature and origin of CO_2 and other carbon oxides in the Uranus system. Additionally, the factor of ~1000 stronger CO_2 asymmetric stretching mode (ν_3), centered near 4.27 μm in crystalline CO_2 ice (e.g., G. B. Hansen 1997; E. Quirico & B. Schmitt 1997a; P. A. Gerakines & R. L. Hudson 2020), is entirely obscured from the ground due to strong absorption by CO_2 and other gases in Earth's atmosphere. Observations made with the NIRSpec spectrograph (2.9–5.1 μm) on the James Webb Space Telescope (JWST) have brought CO_2 and other carbon oxides into focus on the Uranian moon Ariel, revealing prominent CO_2 scattering peaks between 4.15 and 4.26 μm and confirming the presence of CO ice, likely mixed with CO_2 (R. J. Cartwright et al. 2024a). Here, we report JWST/NIRSpec observations of Umbriel, Titania, and Oberon, alongside Ariel. We analyze the spectral signatures of CO_2 and other species on these moons to help decipher the identity, distribution, and origin of carbon oxides in the Uranus system.

2. Data and Methods

2.1. Observations and Data Reduction

JWST/NIRSpec (P. Jakobsen et al. 2022; T. Böker et al. 2023) observed the leading and trailing hemispheres of Ariel, Umbriel, Titania, and Oberon between 2023 September 2 and 2023 September 23 with the G395M/F290LP grating (2.87–5.25 μm; resolving power $R\sim1000$), as part of General Observer Program 1786 (observation details in Table 1). Each observation consisted of four dithers made with NIRSpec's integral field unit (IFU) and the NRSIRS2RAPID readout mode. To achieve comparable signal-to-noise ratio for each observation, we utilized different exposure times to accommodate the differences in intrinsic brightness for each moon, ranging from the brightest moon Titania ($V\sim14$ mag) to the faintest Umbriel ($V\sim15$ mag).

The data were downloaded from the Mikulski Archive for Space Telescopes[13] and then processed by the Science Calibration Pipeline v.1.20.1 with CRDS `context jwst_1464.pmap` to convert raw `uncal` files into `s3d` spectral cubes for all four dithers and for each of the eight observations (H. Bushouse et al. 2023). Default pipeline parameters were used, including NSClean to remove the $1/f$ pattern noise (B. J. Rauscher 2024). Extraction of spectra utilized a template point-spread function (PSF)-fitting routine, following a technique leveraged by past studies that analyzed JWST/NIRSpec data (e.g., A. Souza-Feliciano et al. 2024; R. Brunetto et al. 2025; M. N. De Prá et al. 2025; E. Hénault et al. 2025; L. Markwardt et al. 2025; B. N. Sharkey et al. 2025). To conduct wavelength calibration, a wavelength grid was generated using the `CRVAL3` and `CRDELT3` header keywords, where each wavelength bin was matched to the corresponding spectral slice in the data cube. The centroid position of each target was first estimated by eye (good to within <1 pixel), and we used this centroid as an initial guess in all slices when performing PSF fitting (all four moons are point sources in NIRSpec spaxels, $0\farcs1\times0\farcs1$).

We estimated the background by calculating the median of all spaxels more than 5 spaxels removed from the centroid, which were then subtracted from the spaxels in the slice. Using the median of a moving 21-slice window, we calculated the template PSF. Next, a 9×9 spaxel grid around the centroid of the template PSF was normalized to unity and then fit to the slice in the middle of the 21-slice window using the `scipy.optimize.minimize` function and the Nelder–Mead algorithm. We utilized the flux scaling factor and the background to make the best-fit model. The 1D target spectrum was generated by extracting the flux within a 3.5 pixel radius circular aperture, centered on each slice's centroid. We median combined the four dithers and divided by a median G395M spectrum of P330E, a well-known calibration star (G2V, $V=13.028\pm0.004$ mag; e.g., R. C. Bohlin & A. U. Landolt 2015), in order to remove the solar flux from the target spectrum. P330E spectra were constructed using the same template PSF-fitting routine described above. Uncertainties for all spectra were computed as the median absolute deviation within each wavelength bin, which were propagated to the final solar-divided target spectra (Figure 1).

Band measurements. Identified spectral features were measured by first dividing each by a local linear continuum,

[13] Data doi: 10.17909/nj36-mt02.

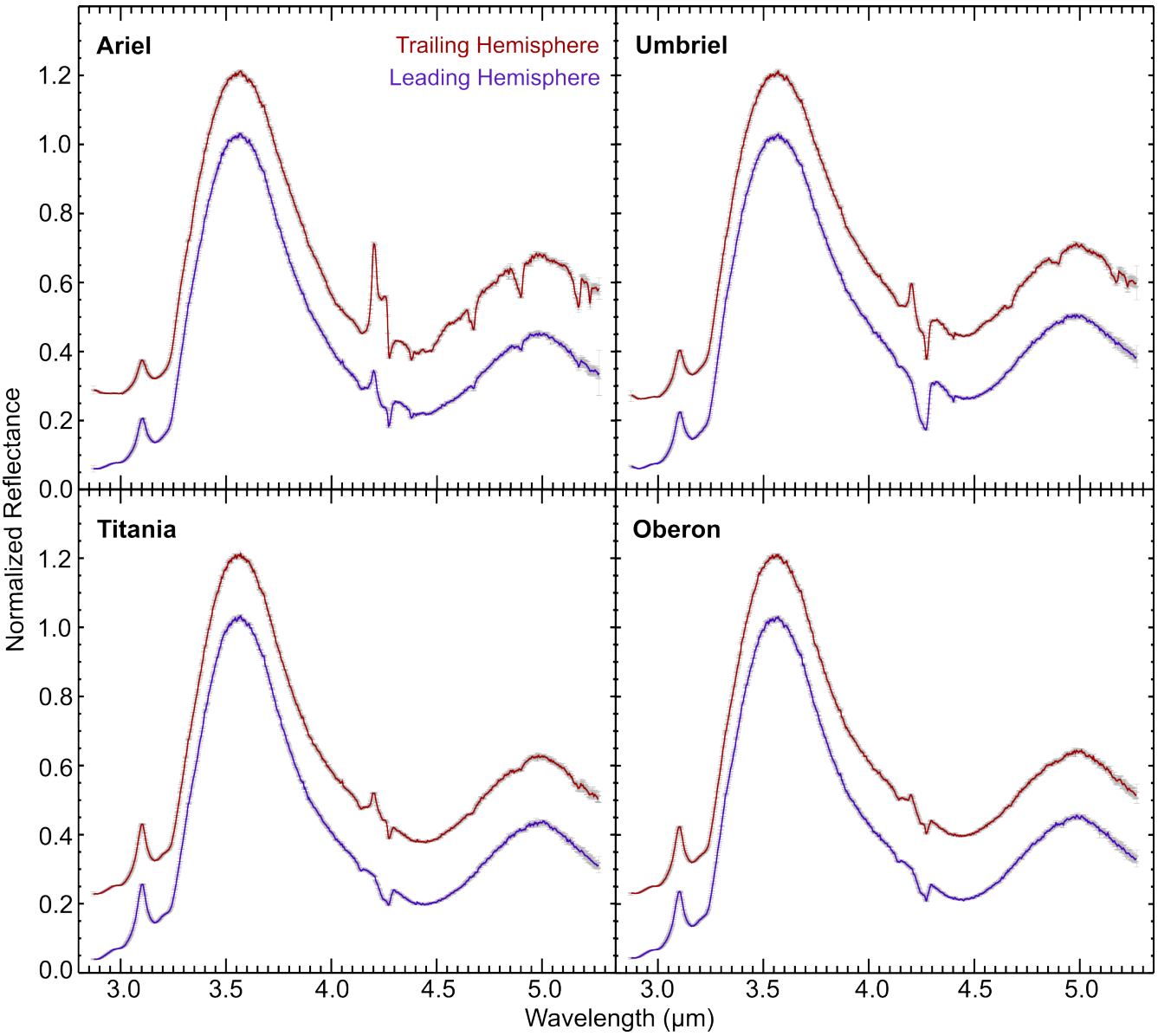

Figure 1. NIRSpec IFU (G395M/F290LP) reflectance spectra and 1σ uncertainties for the leading and trailing hemispheres of Ariel, Umbriel, Titania, and Oberon, normalized to 1 at 3.59 μm and vertically offset for clarity. The spectra of Ariel, originally reported in R. J. Cartwright et al. (2024a), were rereduced here using an updated version of the calibration pipeline, revealing additional spectral structure between 5.1 and 5.25 μm that was not previously presented.

Table 1
JWST/NIRSpec G395M Observation Details

Satellite	Hemisphere	[a]Subobserver Longitude (deg)	Subobserver Latitude (deg)	UT Date	Start Time	Total Exposure Time (s)
Ariel	Trailing	293.4	64.5	2023 Sep 6	19:35:03	3793.1
	Leading	64.0	64.5	2023 Sep 7	17:32:06	3734.8
Umbriel	Trailing	272.2	64.1	2023 Sep 8	15:15:18	8461.6
	Leading	119.8	64.1	2023 Sep 06	21:10:19	8461.6
Titania	Trailing	275.1	63.9	2023 Sep 23	20:13:15	2567.6
	Leading	102.5	64.1	2023 Sep 10	01:03:46	2567.6
Oberon	Trailing	247.1	63.9	2023 Sep 3	8:37:01	3152.2
	Leading	91.5	63.9	2023 Sep 11	00:10:40	3152.2

Note.
[a] Listed values represent the midobservation subobserver longitudes for each moon.

fit to the median value of four to five data points on both sides of each feature (e.g., R. J. Cartwright et al. 2015, 2024a). Continuum-divided, spectral contrast measurements were made by averaging the reflectance values within $\pm$0.001–0.003 μm of the deepest or tallest point in each continuum-divided band (B_c) or peak (P_c), which defines the center of each spectral feature. We utilized standard error propagation procedures to estimate uncertainties for each band and peak measurement (e.g., J. Taylor 1997). Next, the central wavelength position of each feature was assessed manually for quality assurance, before measuring the spectral contrasts of each absorption band ($1 - B_d$) and scattering peak ($P_d - 1$). To quantify the area of each continuum-divided feature, we used the trapezoidal rule and estimated uncertainties with Monte Carlo simulations sampling the 1σ errors for data points within each feature.

2.2. Laboratory Spectra

To better understand the spectral properties of the Uranian moons and the nature of CO_2 on their surfaces, we compared the G395M data to laboratory experiments that measured the spectral properties of CO_2 ice over a range of cryogenic temperatures. We present reflectance spectra of a 10 ± 1 μm thick crystalline CO_2 ice layer deposited onto an organic residue and a 15 ± 1 μm thick crystalline CO_2 ice layer deposited directly onto the Infragold substrate, initially deposited at 50 K, performed with the Irradiation de Glaces et Météorites Analysées par Réflectance (INGMAR), corun by the Institut d'Astrophysique Spatiale and the Laboratoire de physique des deux infinis Irène Joliot-Curie, both at the Université Paris-Saclay (E. Hénault et al. 2025). To do this, gaseous CO_2 was injected into a vacuum chamber ($P \sim 5 \times 10^{-7}$ mbar) and deposited onto an existing $\sim$1 μm thick organic residue, produced from a previous experiment of proton-irradiated CH_3OH:NH_3 ice (subsequently warmed to room temperature), overlying an Infragold substrate initially cooled to 50 K. We also performed this experiment by condensing CO_2 gas directly onto the bare Infragold substrate. The CO_2 samples were then warmed until the CO_2 ice layer sublimated (130 K), with spectra collected at continuous 10 K temperature steps. Furthermore, we compared the G395M data to laboratory reflectance spectra of CO_2 codeposited with H_2O ice ($\sim$1:1) on an Infragold substrate using INGMAR. Here, we report data collected at the initial deposition temperature of 50 K and a later 90 K temperature step.

We also present transmission spectra of a 1 cm thick monocrystal made of pure CO_2, which we compared to the G395M data to investigate weaker features between 3.3–3.4 and 4.8–5.25 μm to help determine whether these features result from thick CO_2 ice deposits. This crystal was grown from the gas phase under a pressure of $\sim$1 bar in a stainless steel cryogenic cell equipped with sapphire windows (experimental setup described by E. Quirico & B. Schmitt 1997b). Spectra were measured at 187 K with a spectral resolution of 1 cm^{-1}. We also compared the G395M data to published laboratory spectra of CO_2 clathrate hydrates measured at 110 K (A. Oancea et al. 2012). Similarly, we compared the G395M data to laboratory spectra of $\sim$1 monolayer (ML) of CO_2 condensed on $\sim$100 nm thick meteorite simulant (amorphous $MgFeSiO_4$) and condensed on the same simulant capped by $\sim$10–80 MLs of amorphous H_2O ice (T. Suhasaria et al. 2025).

3. Results and Analyses

3.1. Detected Spectral Features

All features detected in this study are reported in Table 2. Detection certainty is defined as follows: "secure" detections correspond to features observed on $\geqslant$2 moons at $>3\sigma$ level; "probable" detections correspond to features observed on 1 moon at $>3\sigma$ level; and "tentative" detections correspond to features that have yet to be observed at $>3\sigma$ level and are unmeasured in this study. We also provide a compositional interpretation for all features, along with an interpretation certainty, defined as follows: "confirmed" interpretations represent features with secure detections that are very likely explained by only one compound; "favored" interpretations represent features with probable detections that are likely explained by only one compound; and "ambiguous" interpretations represent all features with tentative detections. Furthermore, all features with secure or probable detections that have multiple compositional interpretations include one favored interpretation with all other interpretations listed as ambiguous.

CO_2 ice. Ariel, Umbriel, Titania, and Oberon exhibit a variety of features resulting from crystalline CO_2 ice, in particular on their trailing hemispheres (Figures 2, 3, and 4, Table 2). The most pronounced examples of these CO_2 features are associated with the ν_3 mode of $^{12}CO_2$ ($\sim$4.2–4.3 μm), representing one of the strongest natural absorbers measured in the laboratory (e.g., D. A. Dows & V. Schettino 1973; U. Fink & G. T. Sill 1982; P. A. Gerakines & R. L. Hudson 2020). Scattering peaks near 4.20 μm (secure detection) are apparent in each trailing hemisphere spectrum, as well as the G395M data for Ariel's leading hemisphere, consistent with the wavelength position of a longitudinal optical (LO) phonon mode observed in crystalline $^{12}CO_2$ ice (I. R. Cooke et al. 2016; T. Suhasaria et al. 2025). In brief, laboratory experiments demonstrate that the ν_3 mode of CO_2 ice expresses an LO mode and a transverse optical (TO) mode, whereby phonons propagate through the crystalline lattice plane parallel and plane perpendicular to incident light, respectively. The trailing hemisphere of Ariel also exhibits a prominent peak centered near 4.25 μm (secure detection) that may represent the largest $^{12}CO_2$ ice Fresnel peak yet observed on an icy body (see Figure A3 in R. J. Cartwright et al. 2024a). Adjacent to these peaks are absorption bands centered near 4.27 μm (secure detection), likely dominated by the TO mode of $^{12}CO_2$ ice (e.g., G. B. Hansen 1997; E. Quirico & B. Schmitt 1997a, 1997b; I. R. Cooke et al. 2016; T. Suhasaria et al. 2025). The leading hemispheres of Umbriel, Titania, and Oberon do not exhibit 4.2 μm scattering peaks but do possess prominent 4.27 μm bands (Figure 2).

The data display additional absorption features near 4.9 and 5.17 μm (both secure detections) on the trailing hemispheres of these moons and on the leading side of Ariel. These features are likely CO_2 BP + P vibrational continua modes corresponding to the ($\nu_1 + \nu_2$; $3\nu_2$) Fermi resonance dyad (R. Bini et al. 1991). Briefly, Fermi resonances occur due to anharmonic interactions where the intensity of a combination or overtone mode is significantly enhanced due to interactions with a fundamental mode with similar energy and identical symmetry.

The G395M data of the inner moons, Ariel and Umbriel, exhibit additional features that are not seen on the outer moons, Titania and Oberon. Many of these features likely

Table 2
Confirmed and Suspected Carbon Oxide Spectral Features

Spectral Feature	Detection Certainty	Interpretation(s)	Interpretation Certainty	Vibrational Modes
3.01 μm band (not measured)	Tentative	CO_2?	Ambiguous	Unknown[a]
3.33 μm band	Secure	$^{12}CO_2$	Favored	Unknown[a] ($\nu_2 + \nu_3$ mag. dipole?; K. Kazakov & A. Vigasin 2021)
		Hydrocarbons?	Ambiguous	ν_3 (e.g., W. Grundy et al. 2002)
3.90 μm band (not measured)	Tentative	H_2CO_3?	Ambiguous	ν(OH) (e.g., M. Moore & R. Khanna 1991)
4.02 μm band	Secure	CO_3	Favored	$\nu_1 + \nu_3$ (R. Hexter 1958)
		H_2CO_3?	Ambiguous	ν(OH) (e.g., M. Moore & R. Khanna 1991)
		CO_2?	Ambiguous	Christiansen feature (M. N. De Prá et al. 2025)
4.20 μm peak	Secure	$^{12}CO_2$	Confirmed	ν_3[a]
4.25 μm peak	Secure	$^{12}CO_2$	Confirmed	ν_3[a]
4.27 μm band	Secure	$^{12}CO_2$	Confirmed	ν_3[a]
4.30 μm band	Probable	$^{12}C^{16}O^{18}O$	Favored	ν_3 (C. J. Bennett et al. 2010b)
		Amorphous $^{12}CO_2$?	Ambiguous	ν_3 (R. M. Escribano et al. 2013)
4.38 μm band	Secure	$^{13}CO_2$	Confirmed	ν_3[a]
4.40 μm band	Secure	$^{13}CO_2$ clathrates	Favored	ν_3 (A. Oancea et al. 2012)
		$^{13}CO_2$?	Ambiguous	ν_3 (This work, Figure 6)
4.41 μm band	Probable	$^{13}C^{16}O^{18}O$?	Favored	ν_3 (M. Loeffler et al. 2005)
		$^{13}CO_2$?	Ambiguous	ν_3 (This work, Figure 6)
		C_XO_2?	Ambiguous	ν_3 (P. Gerakines & M. Moore 2001)
		Nitriles?	Ambiguous	ν_3 (e.g., G. Strazzulla et al. 2007)
4.47 μm band	Probable	$^{13}C^{18}O_2$?	Favored	ν_3 (M. Loeffler et al. 2005)
		Nitriles?	Ambiguous	ν_3 (e.g., G. Strazzulla et al. 2007)
		C_XO_2?	Ambiguous	ν_3 (P. Gerakines & M. Moore 2001)
4.59 μm band	Probable	OCN^-	Favored	ν_3 (R. J. Grim & J. M. Greenberg 1987)
		C_XO_2?	Ambiguous	ν_3 (P. Gerakines & M. Moore 2001)
		CO_2?	Ambiguous	Unknown[a]
4.67 μm band	Secure	^{12}CO	Confirmed	ν_3 (e.g., G. E. Ewing & G. C. Pimentel 1961)
4.78 μm band	Probable	^{13}CO	Favored	ν_3 (e.g., G. E. Ewing & G. C. Pimentel 1961)
		HCN?	Ambiguous	ν_3 (P. A. Gerakines et al. 2022)
4.84 μm band (not measured)	Tentative	CO_2?	Ambiguous	Triphonon (TP)[a,b]
4.90 μm band	Secure	CO_2	Confirmed	Biphonon + phonon (BP + P)[a,b]
		CO_3?	Ambiguous	ν_1 (N. G. Moll et al. 1966)
4.94 μm band (not measured)	Tentative	$^{12}C^{16}O^{18}O$?	Ambiguous	[a,b]
5.02 μm band (not measured)	Tentative	CO_2?	Ambiguous	Unknown[a]
		C_2O?	Ambiguous	ν_1 (e.g., M. E. Jacox et al. 1965)
5.17 μm band	Secure	CO_2	Confirmed	BP + P[a,b]
5.23 μm band	Secure	CO_2	Confirmed	TP[a,b]

Notes.
[a] Interpreted CO_2 features identified using data reported in G. B. Hansen (1997) and E. Quirico & B. Schmitt (1997a, 1997b).
[b] Features between 4.8 and 5.25 μm likely result from the $\nu_2 + \nu_3$; $3\nu_2$ Fermi resonance region (R. Bini et al. 1991).

result from CO_2, including an absorption band near 4.38 μm (secure detection) that we attribute to the ν_3 mode of $^{13}CO_2$ ice. Ariel's and Umbriel's 4.38 μm bands exhibit multilobe structures, with additional features centered near 4.40 μm (secure detection) and 4.41 μm (probable detection). We explore the spectral properties of these multilobe $^{13}CO_2$ features in Section 3.3. The trailing hemispheres of Ariel and Umbriel express a 5.23 μm feature (secure detection) that likely represents a bound triphonon (TP) mode in CO_2 ice, resulting from collective oscillations across a thick crystalline ice lattice (R. Bini et al. 1991). These two moons also exhibit 3.33 μm bands (secure detection) that probably stem from CO_2 ice, but could hypothetically include contributions from hydrocarbons, such as methane and methanol (e.g., W. Grundy et al. 2002; R. N. Clark et al. 2009; E. Dartois et al. 2010; A. Vyjidak et al. 2026). A 4.47 μm band (probable detection) detected on Ariel and possibly on Umbriel's trailing hemisphere, most likely results from thick CO_2 ice deposits (D. A. Dows & V. Schettino 1973), but carbon-chain oxides (P. Gerakines & M. Moore 2001; G. Strazzulla et al. 2007) or even nitrous oxide (N_2O; e.g., G. Strazzulla et al. 2007) are possible (but less likely) alternatives. Similarly, the 4.41 μm feature could hypothetically result from nitriles (CN-bearing organics; e.g., M. P. Bernstein et al. 1997; G. Strazzulla et al. 2007), but the prevalence of other carbon oxide spectral features favors an attribution to CO_2. The 4.41 and 4.47 μm bands could include contributions from $^{13}C^{16}O^{18}O$ and $^{13}C^{18}O_2$, respectively (C. J. Bennett et al. 2010b). Another weak feature near 4.3 μm (probable detection) is only detected on Ariel's leading and trailing hemisphere, embedded on the

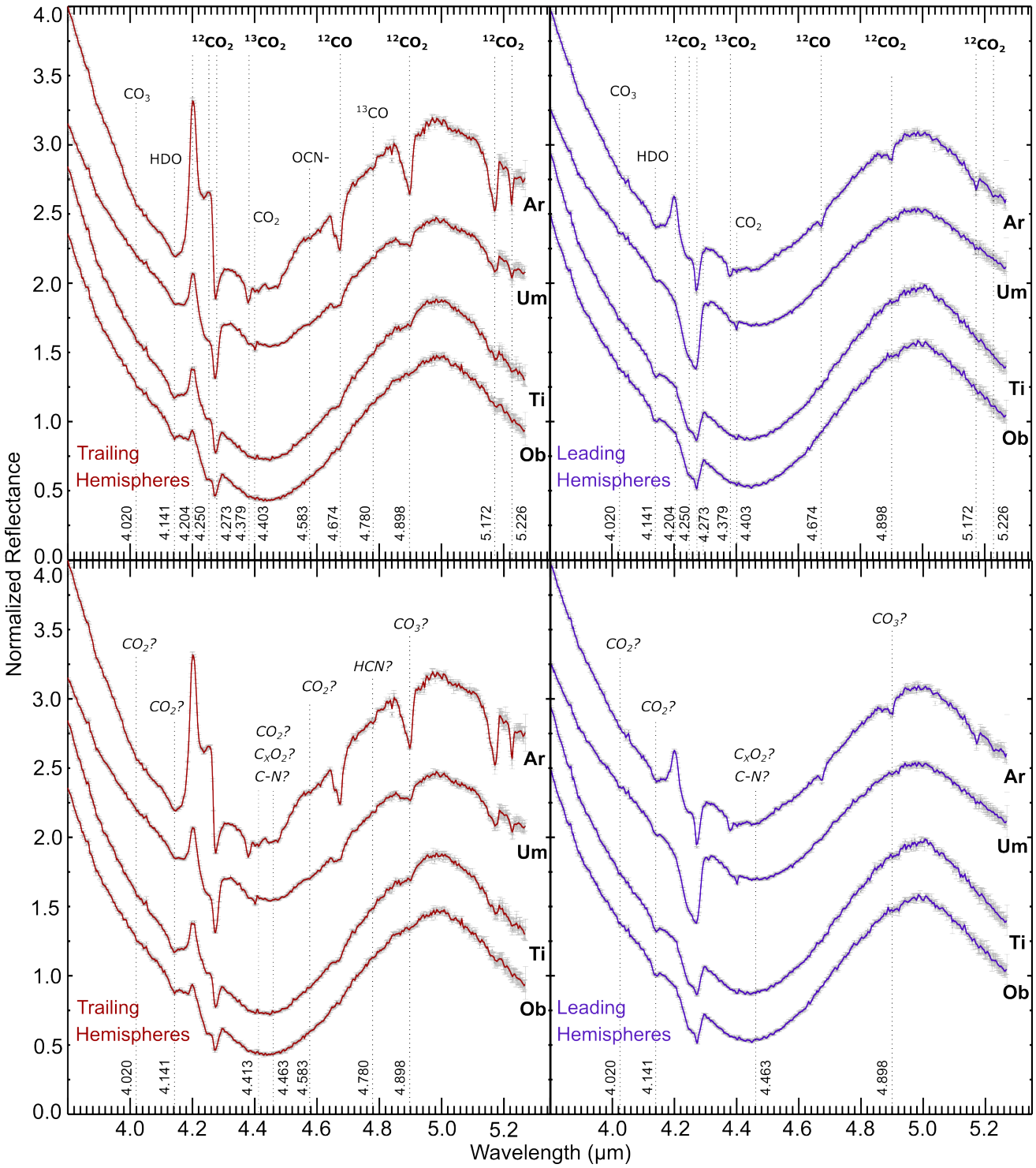

Figure 2. NIRSpec spectra and 1σ uncertainties for Ariel ("Ar"), Umbriel ("Um"), Titania ("Ti"), and Oberon ("Ob"), normalized to 1 at 4.30 μm and offset vertically for clarity (trailing hemisphere data in the left column; leading hemisphere data in the right column). The two upper panels show all features with "confirmed" (bold text) and "favored" compositional interpretations, and the two bottom panels show all features with "ambiguous" (italicized with question marks) compositional interpretations, as described in Section 3.1 and summarized in Table 2. The central wavelengths (microns) for all features are listed vertically along each dotted line and are included in Tables 3, 4, and 5.

long-wavelength shoulder of the 4.27 μm $^{12}CO_2$ feature. This narrow 4.3 μm band could result from $^{12}C^{16}O^{18}O$ (C. J. Bennett et al. 2010b), as well as possibly including minor contributions from amorphous CO_2 (R. M. Escribano et al. 2013). Other features that may result from CO_2 or other carbon oxides, but are too subtle to reliably measure (identified visually, Figure 3), are centered near 3.01, 3.90, 4.84, 4.94, and 5.02 μm (all unmeasured, tentative detections) and discussed further in Section 3.3.

CO ice. The G395M data collected over the trailing hemispheres of these moons (and Ariel's leading hemisphere) show absorption bands centered near 4.67 μm (secure

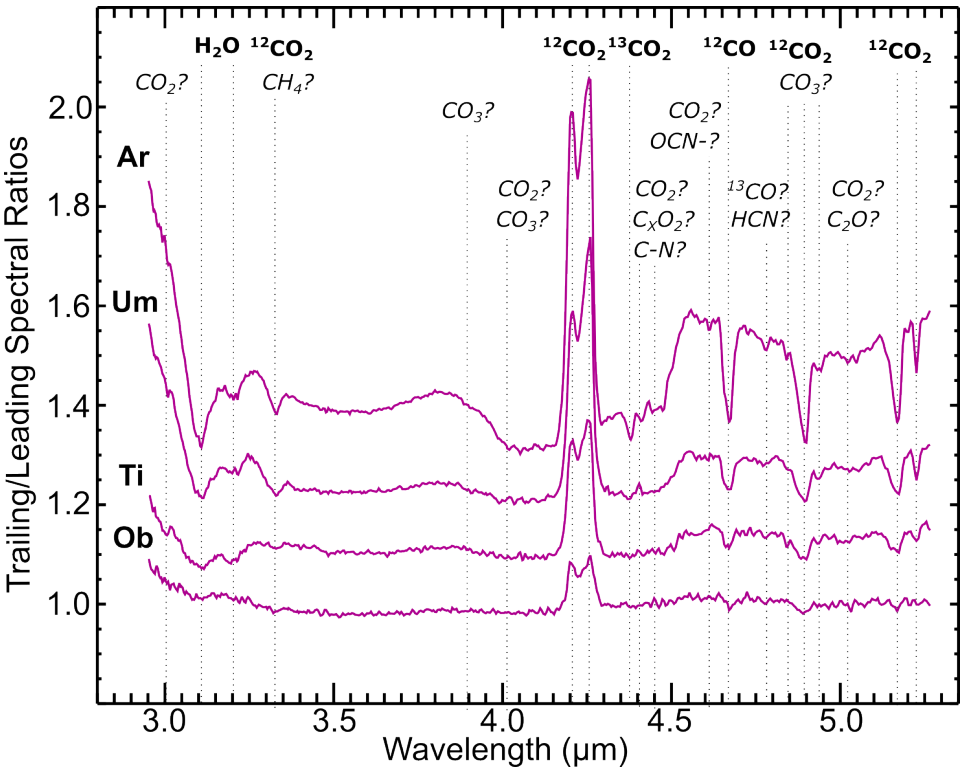

Figure 3. Spectral ratios generated by dividing the trailing hemisphere spectrum by the leading hemisphere spectrum for each moon, offset vertically and with uncertainties omitted for clarity. These ratios highlight the notable hemispherical asymmetries on Ariel ("Ar"), which become progressively weaker on Umbriel ("Um"), Titania ("Ti"), and Oberon ("Ob"). The ratios also reveal subtle features near 3.01, 4.84, 4.93, and 5.02 μm that are not apparent in the nonratio data (unmeasured, tentative detections), possibly associated with thick CO_2 ice deposits (R. J. Cartwright et al. 2024a). An additional weak feature near 3.90 μm (unmeasured, tentative detection) in the spectral ratio of Ariel may result from carbonic acid (Table 2).

detection) that are consistent with the ν_3 mode of ^{12}CO ice (e.g., P. A. Gerakines et al. 2023). At the peak surface temperatures of these moons (80–90 K; R. Hanel et al. 1986; M. M. Sori et al. 2017; S. M. Menten et al. 2024), pure CO should sublimate rapidly (N. Fray & B. Schmitt 2009), indicating it is replenished on short timescales and/or mixed with less volatile compounds. Indeed, the 4.67 μm features are flanked by weaker side bands, likely resulting from CO ice mixed with CO_2 ice (R. J. Cartwright et al. 2024a), as well as possibly H_2O ice (e.g., S. Sandford et al. 1988) and perhaps CO trapped as a guest molecule in a clathrate structure (e.g., E. Dartois 2011). A subtle feature near 4.78 μm (probable detection) on Ariel's trailing hemisphere likely results from the ν_3 mode of ^{13}CO ice (e.g., C. J. Bennett et al. 2010b). Although the ν_3 mode of hydrogen cyanide (HCN) ice overlaps this wavelength range (P. A. Gerakines et al. 2022) and could hypothetically contribute, a C-H stretching mode attributed to HCN near 3.12 μm is apparently absent, as are other HCN ice features. Because of the prevalence of other carbon oxide features in Ariel's G395M data, it seems more plausible that ^{13}CO is the dominant contributor. Additionally, the other moons, which exhibit considerably weaker 4.67 μm ^{12}CO features compared to Ariel, do not express 4.78 μm features, supporting our preferred interpretation of ^{13}CO ice. For more discussion of CO ice in the Uranian system, we refer the reader to prior work that analyzed Ariel's 4.67 μm feature (R. J. Cartwright et al. 2024a).

CO_3-bearing species? All four moons exhibit weak but broad 4.02 μm bands (secure detection) that are generally stronger on their trailing hemispheres, in particular for Ariel (Table 3). These broad features possibly result from a strong $\nu_1 + \nu_3$ combination mode exhibited by CO_3 in carbonate minerals (R. Hexter 1958; J. Bishop et al. 2021), as expressed on main belt asteroid Ceres (e.g., M. C. De Sanctis et al. 2015, 2016; F. G. Carrozzo et al. 2018) and potentially on Jupiter's moon Callisto (R. Johnson et al. 2004; R. J. Cartwright et al. 2024b). Carbonic acid (H_2CO_3) formed via irradiation of H_2O and CO_2 mixtures, also expresses a broad feature attributed to an O-H stretching mode that could hypothetically match the 4.02 μm feature observed on the Uranian moons, but the central wavelength of this H_2CO_3 feature is usually exhibited at shorter wavelengths (3.8–3.9 μm), shifting in response to temperature, contaminant mixing, and other variables (e.g., M. Moore & R. Khanna 1991; W. Hage et al. 1998; P. Gerakines et al. 2000). Indeed, the spectral ratio of Ariel exhibits a subtle 3.9 μm feature (tentative detection) that could hypothetically result from H_2CO_3 (Figure 3). Irradiated CO_2 can also express a 4.89 μm feature attributed to the CO_3 molecule (N. G. Moll et al. 1966; U. Raut & R. Baragiola 2013), which might contribute to the short-wavelength wing of the Uranian moons' 4.9 μm bands (R. J. Cartwright et al. 2024a). We explore potential contributions from carbonate minerals in Section 3.3. We also considered, and ruled out, possible contributions to the 4.02 μm band from sulfur-bearing species, such as sulfur dioxide (SO_2), because there is no reported spectral evidence at other wavelengths for S-bearing species on the Uranian moons, whose surface compositions are apparently dominated by H_2O ice mixed with C-bearing species (e.g., W. Grundy et al. 2006).

Cyanate ions? We note the presence of fairly weak but broad 4.59 μm shoulder features (probable detection) on the

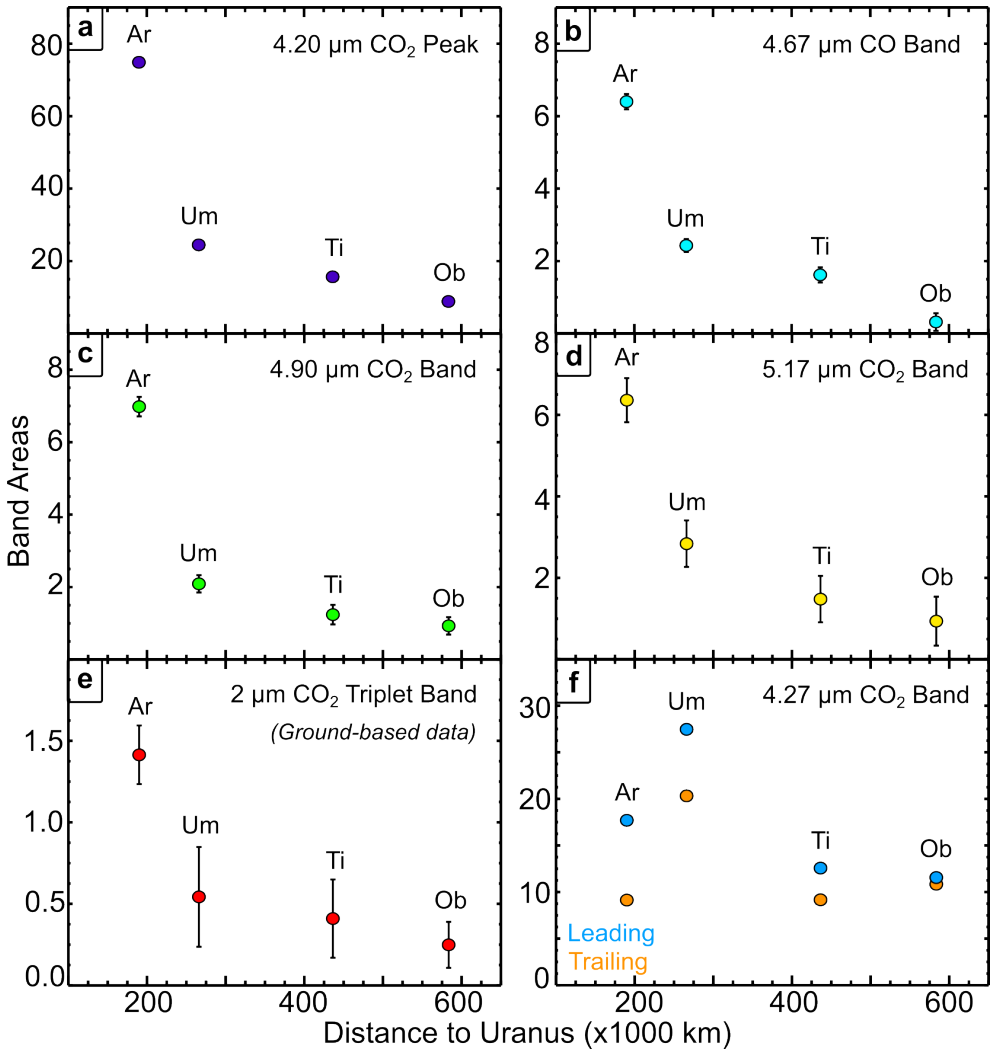

Figure 4. Area measurements and 3σ uncertainties for the (a) 4.20 μm CO_2 peak, (b) 4.67 μm CO band, (c) 4.90 μm CO_2 band, (d) 5.17 μm CO_2 band, (e) the "2 μm CO_2 triplet band" (e.g., W. Grundy et al. 2006), and (f) the 4.27 μm CO_2 band (in some cases, the 3σ uncertainties are smaller than the symbols shown here). All measurements were scaled up by a factor of 1000 (Table 3). For (a)–(e), only trailing hemisphere measurements are shown as most non-Ariel leading hemisphere measurements are ambiguous ($<3\sigma$ detection). For the strong 4.27 μm band (f), measurements of both the leading and trailing hemispheres were made for all four moons. The notable disparity in the apparent trends displayed by the 4.27 μm band measurements compared to the other spectral features highlights the challenges and uncertainties in interpreting this feature (see Section 4.1).

trailing hemispheres of Ariel ($>3\sigma$ detection) and Umbriel ($>2\sigma$ detection; Figure 2, Table 4). Similar ~4.6 μm features, attributed to the cyanate ion (OCN^-), have been identified in JWST/NIRSpec, ground-based, and spacecraft datasets for Jupiter's moon Callisto (e.g., T. McCord et al. 1998b; R. J. Cartwright et al. 2020b, 2024b), the interstellar medium (ISM) and protoplanetary disks (e.g., Y. Pendleton et al. 1999; R. Hudson et al. 2001; M. K. McClure et al. 2023; J. Sturm et al. 2023; A. Potapov et al. 2025), young stellar objects (A. Boogert et al. 2022), and some trans-Neptunian objects (S. Cryan et al. 2025). Laboratory experiments have shown that OCN^- forms via irradiation of mixed NH_3, CO (and/or CO_2), and H_2O substrates at temperatures relevant to the outer solar system and the ISM (e.g., F. Van Broekhuizen et al. 2004; C. Bennett et al. 2010a; Y.-J. Chen et al. 2011), and can also form thermally via interactions between H_2O and isocyanic acid (HNCO) at temperatures above 110 K (S. Raunier et al. 2003). Spectral hints of NH_3, and/or NH_4-bearing species, have been identified previously on the Uranian moons (J. M. Bauer et al. 2002; R. J. Cartwright et al. 2018, 2020c, 2023; R. A. DeColibus et al. 2023), supporting the possibility that weak 4.59 μm features may result from OCN^-, formed via irradiation of NH-bearing species mixed with CO_2 and H_2O in their regoliths. Of note, we found no trace of a ν_3 stretching mode expressed by NH_3 and other NH-bearing compounds near 2.96 μm in the G395M data, consistent with other studies that looked for this spectral feature on Ariel (R. J. Cartwright et al. 2024a) and Pluto's moon Charon (S. Protopapa et al. 2024). Alternatively, perhaps the 4.59 μm band results from a poorly characterized CO_2 "shoulder" feature (see Figure 2 in R. J. Cartwright et al. 2024a), which appears to be present in some laboratory datasets (G. B. Hansen 1997). A more complete exploration of OCN^- versus CO_2 contributions near 4.59 μm is beyond the scope of this study and left for future work.

H_2O and HDO ice. The Uranian moons exhibit multiple strong features indicative of crystalline H_2O ice. All four moons display prominent H_2O ice Fresnel features in the 2.90–3.25 μm region (R. Mastrapa et al. 2009), typified by scattering peaks near 3.10 μm, attributed to the ν_3 TO mode of

Table 3
Measurements of Carbon Oxide Spectral Features on Ariel, Umbriel, Titania, and Oberon

Feature Name	Satellite	Hemisphere	Feature Center (μm)	Wavelength Range (μm)	Spectral Contrast (%)	Band Area (10^{-3} μm)	$>3\sigma$ Spectral Contrast and Band Area?
4.02 μm band	Ariel	Trailing	4.02	3.96–4.11	7.83 ± 0.58	59.18 ± 0.82	Yes
		Leading	”	”	3.97 ± 0.33	30.12 ± 0.77	Yes
	Umbriel	Trailing	”	”	1.82 ± 0.47	7.75 ± 0.61	Yes
		Leading	”	”	1.70 ± 0.56	0.28 ± 0.67	No
	Titania	Trailing	”	”	2.42 ± 0.42	16.75 ± 0.64	Yes
		Leading	”	”	2.44 ± 0.52	11.47 ± 0.72	Yes
	Oberon	Trailing	”	”	2.16 ± 0.53	9.35 ± 0.81	Yes
		Leading	”	”	1.74 ± 0.65	5.69 ± 0.70	No
4.20 μm peak	Ariel	Trailing[a]	4.204	4.152–4.276	127.95 ± 1.11	74.86 ± 0.14	Yes
		Trailing[a]	4.252	4.152–4.276	82.42 ± 1.10	74.86 ± 0.14	Yes
		Leading	”	”	39.43 ± 0.82	19.64 ± 0.10	Yes
	Umbriel	Trailing	4.205	4.152–4.276	46.88 ± 1.08	24.47 ± 0.08	Yes
		Leading	…	…	…	…	No
	Titania	Trailing	4.204	4.152–4.276	29.29 ± 0.58	15.66 ± 0.05	Yes
		Leading	…	…	…	…	No
	Oberon	Trailing	4.204	4.152–4.276	18.43 ± 0.82	8.86 ± 0.09	Yes
		Leading	…	…	…	…	No
4.27 μm band	Ariel	Trailing	4.274	4.258–4.303	42.40 ± 0.51	9.14 ± 0.05	Yes
		Leading	4.272	4.200–4.302	37.91 ± 0.85	17.70 ± 0.06	Yes
	Umbriel	Trailing	4.273	4.200–4.302	44.58 ± 0.31	20.32 ± 0.06	Yes
		Leading	4.269	4.188–4.302	48.05 ± 0.31	27.46 ± 0.06	Yes
	Titania	Trailing	4.273	4.200–4.302	23.20 ± 0.58	9.17 ± 0.07	Yes
		Leading	”	”	23.66 ± 0.61	12.57 ± 0.06	Yes
	Oberon	Trailing	”	”	21.58 ± 0.63	10.84 ± 0.07	Yes
		Leading	”	”	23.54 ± 0.48	11.56 ± 0.07	Yes
4.67 μm band	Ariel	Trailing	4.674	4.640–4.706	23.47 ± 0.42	6.40 ± 0.07	Yes
		Leading	”	”	7.41 ± 1.14	1.01 ± 0.08	Yes
	Umbriel	Trailing	4.675	”	7.48 ± 0.63	2.43 ± 0.06	Yes
		Leading	”	”	1.60 ± 0.67	0.38 ± 0.07	No
	Titania	Trailing	4.671	”	5.26 ± 0.51	1.62 ± 0.07	Yes
		Leading	”	”	1.45 ± 0.56	0.55 ± 0.08	No
	Oberon	Trailing	”	”	2.28 ± 0.53	0.32 ± 0.08	Yes
		Leading	…	…	…	…	No
4.90 μm band	Ariel	Trailing	4.898	4.845–4.927	20.79 ± 0.61	6.98 ± 0.09	Yes
		Leading	4.901	”	6.30 ± 0.59	1.73 ± 0.09	Yes
	Umbriel	Trailing	4.900	”	6.05 ± 0.67	2.09 ± 0.08	Yes
		Leading	4.901	”	1.06 ± 0.57	0.41 ± 0.08	No
	Titania	Trailing	4.901	”	3.83 ± 0.89	1.24 ± 0.09	Yes
		Leading	”	”	0.99 ± 0.71	0.37 ± 0.09	No
	Oberon	Trailing	4.895	”	2.03 ± 0.63	0.93 ± 0.08	Yes
		Leading	…	…	…	…	No
5.17 μm band	Ariel	Trailing	5.171	5.115–5.190	21.49 ± 1.66	6.36 ± 0.18	Yes
		Leading	”	”	5.72 ± 1.74	0.81 ± 0.21	Yes
	Umbriel	Trailing	”	”	8.58 ± 2.38	2.84 ± 0.19	Yes
		Leading	”	”	2.30 ± 1.75	0.62 ± 0.20	No
	Titania	Trailing	”	”	4.59 ± 1.34	1.48 ± 0.19	Yes
		Leading	…	…	…	…	No
	Oberon	Trailing	5.171	5.115–5.190	3.14 ± 1.23	0.94 ± 0.20	No
		Leading	…	…	…	…	No

Note.
[a] The 4.20 and 4.25 μm peaks are convolved, and we report the same area for both features.

H_2O ice, flanked by a weaker peak near 2.95 μm, attributed to the ν_3 LO mode and the ν_1 out-of-phase mode, and another peak near 3.2 μm, attributed to the ν_1 in-phase mode (J. t. Bertie & E. Whalley 1964; E. Whalley 1977; R. Mastrapa et al. 2009). The H_2O ice Fresnel region is stronger on the leading hemispheres of these satellites, with notably stronger 3.1 μm Fresnel peaks on the leading sides of the inner moons, Ariel and Umbriel, but only minor differences between the leading and trailing hemispheres of the outer moons, Titania and Oberon (Table 5). The 3.6 μm continuum peak exhibits similar hemispherical trends on these moons, with more prominent differences for the inner moons, Ariel and Umbriel, compared to the outer moons, Titania and Oberon (Table 5). Furthermore, the strongest H_2O ice features on

Table 4
Measurements of Likely Carbon Oxide Spectral Features on Ariel and Umbriel

Feature Name	Satellite	Hemisphere	Feature Center (μm)	Wavelength Range (μm)	Spectral Contrast (%)	Band Area (10^{-4} μm)	$>3\sigma$ Spectral Contrast and Band Area?
3.33 μm band	Ariel	Trailing	3.331	3.328–3.357	2.73 ± 0.34	3.78 ± 0.43	Yes
		Leading	…	…	…	…	No
	Umbriel	Trailing	3.331	3.328–3.357	1.50 ± 0.33	1.14 ± 0.35	Yes
		Leading	…	…	…	…	No
4.30 μm band	Ariel	Trailing	4.298	4.292–4.302	2.96 ± 0.35	0.92 ± 0.26	Yes
		Leading	”	”	2.75 ± 0.35	1.00 ± 0.26	Yes
	Umbriel	Trailing	…	…	…	…	No
		Leading	…	…	…	…	No
4.38 μm band	Ariel	Trailing	4.378	4.365–4.391	11.80 ± 1.10	1.76 ± 0.05	Yes
		Leading	”	”	8.84 ± 0.74	1.18 ± 0.05	Yes
	Umbriel	Trailing	4.379	4.367–4.390	2.28 ± 0.51	0.27 ± 0.03	Yes
		Leading	4.381	4.367–4.390	1.55 ± 0.77	0.21 ± 0.04	No
4.40 μm lobe[a]	Ariel	Trailing	4.403	4.393–4.429	3.16 ± 0.51	8.06 ± 0.43	Yes
		Leading	”	”	2.25 ± 0.69	2.37 ± 0.46	Yes
	Umbriel	Trailing	4.401	4.388–4.422	5.43 ± 0.52	3.52 ± 0.36	Yes
		Leading	4.398	4.389–4.412	3.89 ± 1.24	3.87 ± 0.38	Yes
4.41 μm lobe	Ariel	Trailing	4.412	4.393–4.429	5.42 ± 0.55	8.06 ± 0.43	Yes
		Leading	4.414	4.393–4.421	2.06 ± 0.53	2.37 ± 0.46	Yes
	Umbriel	Trailing	4.416	4.388–4.422	0.26 ± 0.45	3.52 ± 0.36	No
		Leading	…	…	…	…	No
4.47 μm band	Ariel	Trailing	4.468	4.430–4.495	6.22 ± 0.60	28.79 ± 0.66	Yes
		Leading	4.463	”	2.25 ± 0.69	9.86 ± 0.87	Yes
	Umbriel	Trailing	”	”	1.56 ± 0.58	7.77 ± 0.59	No
		Leading	”	”	0.45 ± 0.71	5.67 ± 0.59	No
4.59 μm band	Ariel	Trailing	4.591	4.552–4.640	2.40 ± 0.43	15.14 ± 0.79	Yes
		Leading	”	”	1.10 ± 0.44	3.73 ± 0.89	No
	Umbriel	Trailing	”	”	1.35 ± 0.67	8.20 ± 0.80	No
		Leading	…	…	…	…	No
4.78 μm band	Ariel	Trailing	4.781	4.764–4.797	3.69 ± 0.88	2.54 ± 0.51	Yes
		Leading	…	…	…	…	No
	Umbriel	Trailing	…	…	…	…	No
		Leading	…	…	…	…	No
5.23 μm band	Ariel	Trailing	5.226	5.209–5.237	12.36 ± 1.94	1.34 ± 0.18	Yes
		Leading	…	…	…	…	No
	Umbriel	Trailing	5.227	5.209–5.237	5.19 ± 1.62	0.68 ± 0.18	Yes
		Leading	…	…	…	…	No

Note.
[a] The 4.40 and 4.41 μm lobes are convolved, and we report the same area for both features.

these four moons are associated with the leading hemisphere of Titania, whereas the weakest H_2O ice features are associated with the trailing hemispheres of Ariel and Umbriel. Ground-based observations of the Uranian moons, made with the SpeX spectrograph on NASA's IRTF (J. T. Rayner et al. 2003), also show stronger H_2O ice features on the leading hemispheres of these moons, but with Ariel exhibiting the strongest overall H_2O ice features, not Titania (W. Grundy et al. 2006; R. J. Cartwright et al. 2015, 2018). We discuss this disparity in Section 4.2.

All of the G395M data display absorption features near 4.14 μm. Similar 4.14 μm bands in Saturn's icy rings and ring moons (R. N. Clark et al. 2019; M. Hedman et al. 2024), on icy moons at Saturn (R. N. Clark et al. 2019; M. E. Brown et al. 2025), and putatively on Ariel (R. J. Cartwright et al. 2024a) have been attributed to "semiheavy" water in ordinary H_2O ice, whereby deuterium (D) substitutes for one of the hydrogen atoms in water molecules. However, the proximity of strong $^{12}CO_2$ ice scattering peaks near 4.2 μm makes assessment of potential HDO features difficult, especially on CO_2-rich Ariel and Umbriel where measurements of the 4.14 μm band are likely unreliable. On Titania and Oberon, however, where CO_2 ice features are weaker, the 4.14 μm band may be adequately isolated from nearby CO_2 features to permit robust measurements. On these two outer moons, we find that the 4.14 μm feature is slightly stronger on their leading sides ($<2\sigma$ difference). Furthermore, when comparing the moons, Titania's leading hemisphere exhibits the strongest 4.14 μm band, seemingly consistent with the stronger H_2O ice Fresnel region and 3.6 μm continuum peak on the leading side of this moon. We refer the reader to prior work for deeper investigation of H_2O ice on the Uranian moons (e.g., W. Grundy et al. 2006; R. J. Cartwright et al. 2015, 2018, 2020a), and to a complementary study that calculates $D/(D+H)$ ratios using the G395M data of Titania reported here, modeled with new H_2O ice and HDO ice optical constants measured in the laboratory (S. Tegler et al. 2026).

Table 5
Measurements of H_2O Ice Spectral Features on Ariel, Umbriel, Titania, and Oberon

Feature Name	Satellite	Hemisphere	Feature Center (μm)	Wavelength Range (μm)	Spectral Contrast (%)	Band Area (10^{-3} μm)	$>3\sigma$ Spectral Contrast and Band Area?
3.10 μm peak	Ariel	Trailing	3.102	3.014–3.168	66.00 ± 1.08	38.53 ± 0.12	Yes
		Leading	3.104	3.014–3.168	94.30 ± 1.97	55.33 ± 0.13	Yes
	Umbriel	Trailing	3.106	3.014–3.168	82.32 ± 2.66	49.65 ± 0.11	Yes
		Leading	3.107	3.014–3.168	96.80 ± 3.42	60.17 ± 0.12	Yes
	Titania	Trailing	3.104	3.014–3.168	134.81 ± 3.14	79.25 ± 0.09	Yes
		Leading	”	”	139.24 ± 3.34	82.32 ± 0.14	Yes
	Oberon	Trailing	”	”	132.34 ± 3.37	79.41 ± 0.15	Yes
		Leading	”	”	134.47 ± 3.34	80.36 ± 0.16	Yes
3.60 μm cont. peak	Ariel	Trailing	3.569	3.3–3.9	116.80 ± 0.50	424.71 ± 0.23	Yes
		Leading	3.564	3.3–3.9	122.62 ± 0.52	439.51 ± 0.21	Yes
	Umbriel	Trailing	3.569	3.3–3.9	106.22 ± 0.57	394.55 ± 0.19	Yes
		Leading	”	”	109.66 ± 0.43	403.51 ± 0.19	Yes
	Titania	Trailing	3.557	3.3–3.9	138.35 ± 0.55	490.38 ± 0.17	Yes
		Leading	3.569	3.3–3.9	140.90 ± 0.55	498.05 ± 0.22	Yes
	Oberon	Trailing	”	”	126.32 ± 0.51	455.81 ± 0.23	Yes
		Leading	”	”	128.66 ± 0.56	461.86 ± 0.22	Yes
4.14 μm band	Ariel[a]	Trailing	4.141	4.124–4.156	2.60 ± 0.60	0.46 ± 0.05	Yes
		Leading	”	”	2.80 ± 0.84	0.50 ± 0.04	Yes
	Umbriel[a]	Trailing	”	”	2.14 ± 0.67	0.34 ± 0.04	Yes
		Leading	”	”	2.13 ± 0.56	0.40 ± 0.04	Yes
	Titania	Trailing	”	”	3.03 ± 0.11	0.42 ± 0.04	Yes
		Leading	”	”	3.71 ± 0.63	0.59 ± 0.04	Yes
	Oberon	Trailing	”	”	2.52 ± 0.66	0.36 ± 0.04	Yes
		Leading	”	”	2.80 ± 0.63	0.51 ± 0.04	Yes

Note.
[a] The 4.14 μm bands for the inner moons Ariel and Umbriel are likely contaminated by contributions from nearby CO_2 features. For completeness, we include measurements of the 4.14 μm band on Ariel and Umbriel, with the caveat that they are probably unreliable.

3.2. Spectral Feature Measurements

Secure detections. The trailing hemispheres of Ariel, Umbriel, Titania, and Oberon exhibit prominent 4.02, 4.14, 4.20, 4.27, 4.67, and 4.90 μm absorption bands and 3.10 μm Fresnel peaks and 3.60 μm continuum peaks, with $>3\sigma$ detection of both band depths or peak heights (“spectral contrast”) and areas for these features (Tables 3 and 5). The trailing hemispheres of Ariel, Umbriel, and Titania also exhibit prominent 5.17 μm features ($>3\sigma$ detection), whereas this feature is slightly weaker on Oberon’s trailing side ($>2\sigma$). Similarly, the leading hemisphere of Ariel exhibits all six of these features ($>3\sigma$), but they are considerably weaker than the same features on its trailing hemisphere. The leading hemispheres of the other three moons exhibit strong 4.27 μm bands ($>3\sigma$), and Titania ($>3\sigma$), Umbriel ($>2\sigma$), and Oberon ($>2\sigma$) exhibit broad 4.02 μm bands on their leading sides as well. The leading hemispheres of Umbriel and Titania also express modest 4.67 μm features ($>2\sigma$). The trailing hemispheres of Ariel and Umbriel express absorption features centered near 3.33, 4.38, 4.40, and 5.23 μm ($>3\sigma$). The leading hemisphere of Ariel exhibits 4.38 and 4.4 μm features ($>3\sigma$). Ariel's 4.20 and 4.25 μm scattering peaks are convolved, and we report the same area for both features.

Probable detections. Weaker features near 4.30, 4.41, 4.47, 4.59, and 4.78 μm are detected on the trailing hemisphere of Ariel, and the 4.30, 4.41, and 4.47 μm features ($>3\sigma$) and a 4.59 μm band ($>2\sigma$) are also present on Ariel’s leading side (Table 4). The 4.41, 4.47, and 4.59 μm features are present on Umbriel’s trailing hemisphere but are detected at a lower confidence level ($>2\sigma$), thereby limiting robust measurements of these three features to only one moon (Ariel), making their detection “probable” and not “secure” (see opening paragraph of Section 3.1). The 4.40 and 4.41 μm features are convolved, and we report the same area for both.

Thus, Ariel’s trailing hemisphere exhibits a rich variety of prominent and subtle spectral features likely resulting from carbon oxides, whereas its leading hemisphere, and the trailing hemisphere of Umbriel, express weaker versions of many of the same features. The trailing hemispheres of Titania and Oberon exhibit a small number of these spectral features, whereas their leading sides only exhibit 4.02 and 4.27 μm bands. We compare band and peak area measurements for the most prominent CO_2 (4.20, 4.27, 4.90, and 5.17 μm) and CO (4.67 μm) features to ground-based measurements of the CO_2 triplet band to discern relevant trends in the distribution of these species (Figure 4) and discuss the measurements further in Section 4.1.

3.3. Comparison to Laboratory Spectra

After H_2O ice, the spectral properties of Ariel and the other large Uranian moons are largely defined by CO_2, dominated by a few prominent features associated with its ν_3 mode and complemented by a rich variety of more subtle CO_2 features. To help isolate the signature of CO_2 features outside the core of the $^{12}CO_2$ ν_3 mode (4.2–4.3 μm), we generated spectral ratios by dividing the trailing hemisphere spectrum by the

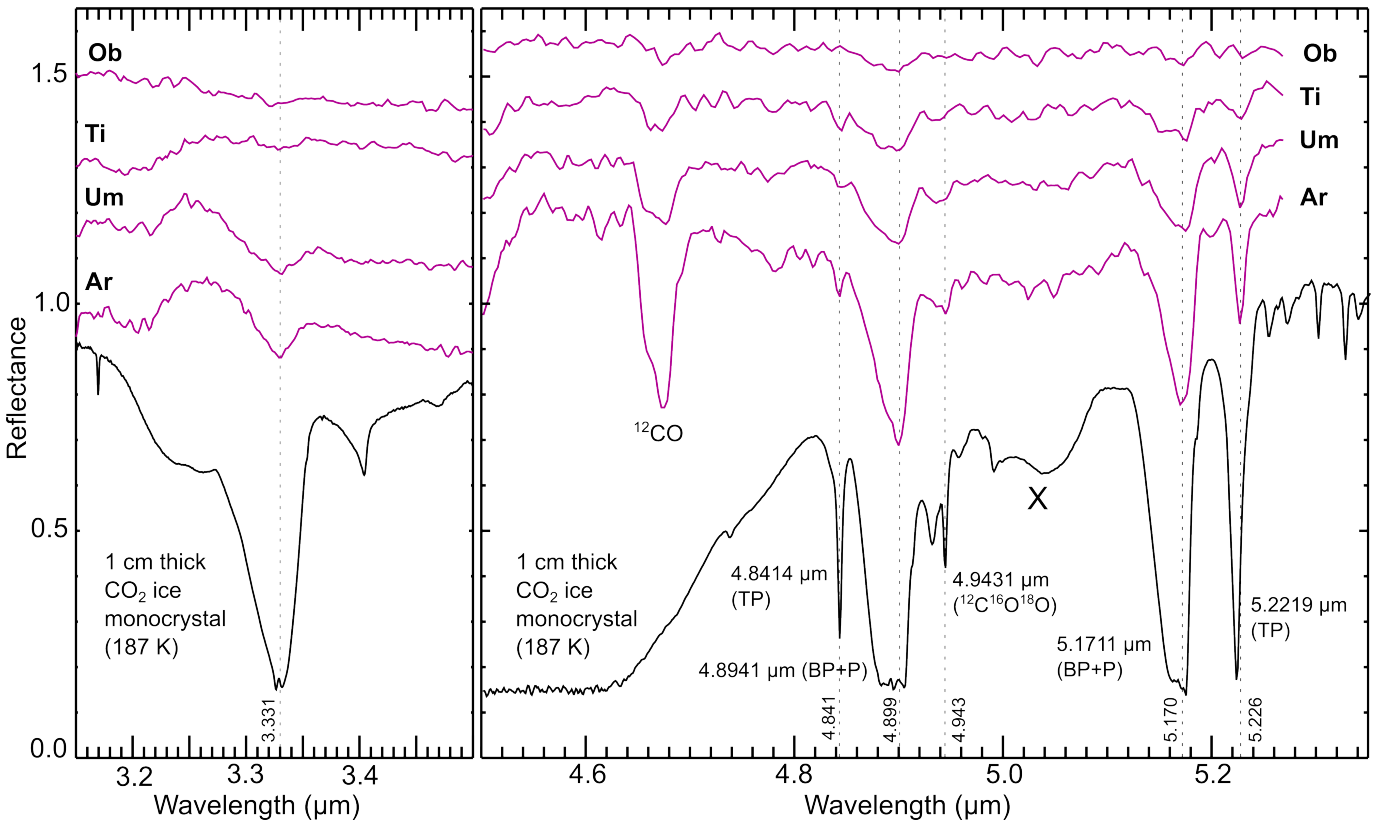

Figure 5. Left: Close up of the trailing/leading spectral ratios (3.15 - 3.5 μm) for Ariel ("Ar"), Umbriel ("Um"), Titania ("Ti"), and Oberon ("Ob") compared to a laboratory spectrum of an ~1 cm thick monocrystal of CO_2 ice (187 K), offset vertically for clarity. The central wavelength (microns) of the 3.331 μm feature (secure detection; Table 2) identified on Ariel and Umbriel (listed vertically along the dotted line) is in close agreement with the center of a strong absorption feature in the laboratory spectrum. Right: the same spectral ratios showing spectral features near 4.899, 5.171, and 5.226 μm (secure detections; Table 2) that align well with the positions of TP and BP + P modes identified in crystalline CO_2 ice (R. Bini et al. 1991), although the 5.226 μm feature observed on the Uranian moons appears to be shifted to slightly longer wavelengths compared to the TP mode expressed by the laboratory data (~5.222 μm). The laboratory spectrum is saturated between ~3.95 and 4.65 μm due to strong absorption by the CO_2 ν_3 mode. The Uranian moon spectral ratios exhibit an additional feature near 4.67 μm (Table 3) that is absent from crystalline CO_2 ice and results from ^{12}CO ice. Other features exhibited by the Uranian moons (especially Ariel) near 4.84 and 4.94 μm aligns well with a TP mode in $^{12}CO_2$ and a $^{12}C^{16}O^{18}O$ feature, respectively (tentative detections; Table 2). Additional "continuum" structure in the laboratory spectrum may result from unattributed modes in crystalline CO_2 ice (example marked with an "×" near 5.02 μm).

leading hemisphere spectrum for each moon (Figure 3). To better understand the nature of combination and overtone modes in CO_2 ice between 3.3–3.4 μm and between 4.8–5.3 μm, we compared the spectral ratios for all four moons to a spectrum of an ~1 cm thick monocrystal of CO_2 ice, generated using procedures described in Section 2.2 (Figure 5). To investigate the nature of isotopologues and help determine whether other carbon oxides are present, we compared the G395M data of Ariel and Umbriel, the two moons with the strongest CO_2 features, to laboratory absorbance and reflectance spectra of crystalline CO_2 ice and CO_2 clathrates (Figures 6, 7, 8, and 9).

Trailing/leading spectral ratios compared to thick cell CO_2 ice samples. Optically thick CO_2 ice substrates measured in the laboratory express a variety of weak absorption features between 4.8 and 5.25 μm, resulting from the $\nu_1 + \nu_2$ and $3\nu_2$ vibration modes in Fermi resonance (D. A. Dows & V. Schettino 1973; R. Bini et al. 1991; E. Quirico & B. Schmitt 1997a, 1997b). Several bands are observed in this wavelength region, including a broad continuum of absorption due to the overlap of the $\nu_2(\vec{k_1}) + \nu_2(\vec{k_2}) + \nu_2(\vec{k_3})$ $(\vec{k_1} + \vec{k_2} + \vec{k_3} = \mathbf{0})$ and the $\nu_1(\vec{k_1}) + \nu_2(\vec{k_2})$ $(\vec{k_1} + \vec{k_2} = \mathbf{0})$ continua. Identified features include two sharp TP modes at 4.842 and 5.222 μm, as well as two BP + P bands near 4.894 and 5.171 μm that are both saturated in the presented laboratory spectrum (Figure 5). The laboratory data also show two weak and narrow features near 4.902 μm (merged in the shoulder of the BP + P band) and 4.943 μm, which are due to the $^{13}CO_2$ and $^{12}C^{16}O^{18}O$ isotopologues, respectively. In particular for Ariel and Umbriel, the G395M data and spectral ratios show features that are well matched by the TP and BP + P modes (secure detections), along with the presence of a weaker feature near 4.94 μm (tentative detection) that may result from $^{12}C^{16}O^{18}O$ ice (Table 2). The expression of these TP and BP + P features very likely confirms that crystalline CO_2 ice is present on the surface of Ariel and the other moons, supporting earlier ground-based studies that made similar assertions based on the presence of the CO_2 triplet band (e.g., W. Grundy et al. 2003). Although these moons' 4.90 μm bands are likely dominated by CO_2 ice, a 4.89 μm feature exhibited by CO_3, formed in irradiated CO_2 substrates (N. G. Moll et al. 1966; U. Raut & R. Baragiola 2013), cannot be ruled out as a minor contributor to the short-wavelength wing of the 4.90 μm bands (R. J. Cartwright et al. 2024a).

We note additional, subtle structure between ~5 and 5.1 μm in the G395M data, especially of Ariel, roughly centered near 5.02 μm (tentative detection; Table 2). The CO_2 monocrystal expresses several other weak absorption features within this same wavelength range that still lack attribution to specific vibrational modes (example labeled with an "×" in Figure 5).

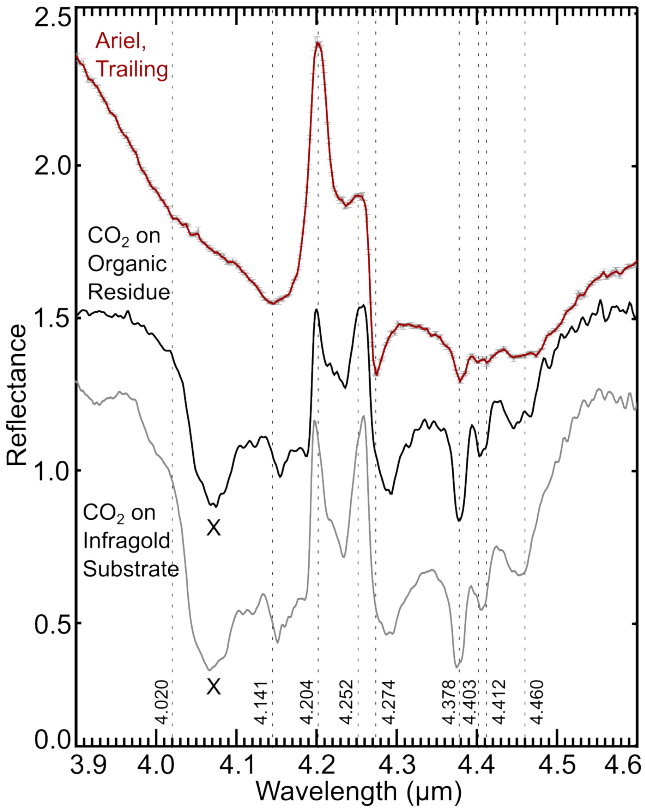

Figure 6. G395M data of Ariel's trailing hemisphere compared to laboratory reflectance data of an ~10 μm thick layer of CO_2 ice deposited on an irradiated organic residue and ~15 μm thick layer of CO_2 ice deposited directly onto an Infragold substrate (both warmed up to 90 K), arbitrarily scaled and offset vertically for clarity. The central wavelengths (microns) for features with secure, probable, and tentative detections (Table 2) in the Ariel spectrum are listed vertically along each dotted line (measurements summarized in Tables 3, 4, and 5). A possible Christiansen feature expressed by the laboratory spectra (marked with an "×") is notably absent from G395M data of Ariel and the other large moons.

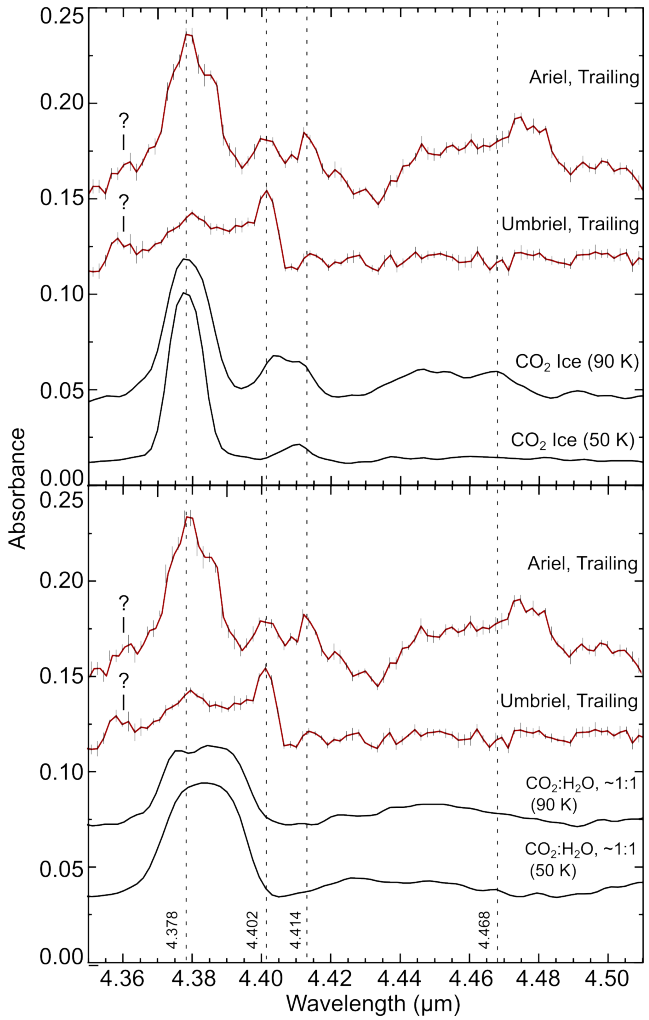

Figure 7. Top: absorbance spectra (–log(reflectance)) of a thick CO_2 ice layer deposited at 50 K and warmed up to 90 K on an organic residue, measured using INGMAR (e.g., E. Hénault et al. 2025). These laboratory spectra are compared to G395M reflectance data of Ariel trailing and Umbriel trailing, converted to absorbance (–log(reflectance)) and offset vertically for clarity. Bottom: CO_2 ice codeposited with H_2O ice at 50 K and then warmed up to 90 K, compared to the same Ariel trailing and Umbriel trailing data in the top plot. Dashed lines highlight spectral features identified on Ariel, some of which are also seen on Umbriel, with the approximate central wavelength listed vertically along the lines. The 4.38, 4.40, and 4.41 μm features identified on Ariel match similar spectral features in the CO_2 ice layer deposited on an organic residue, in particular at 90 K, comparable to the estimated peak temperatures on the Uranian moons (R. Hanel et al. 1986; M. M. Sori et al. 2017). The match to the Umbriel data, however, is less certain. Additional structure in the CO_2 ice laboratory spectrum (90 K) provides a rough match to the short-wavelength side of Ariel's ~4.47 μm feature, hinting that CO_2 might contribute to this feature, along with other compounds. In contrast, the CO_2:H_2O mixtures do not provide reasonable matches to either Ariel's or Umbriel's 4.38 μm features and do not reproduce the features near 4.4, 4.41, or 4.47 μm. None of the laboratory spectra are able to reproduce a small feature near 4.36 μm detected in the Ariel and Umbriel data (labeled with question marks).

Thus, perhaps the subtle structure between 5 and 5.1 μm results from weak and unattributed CO_2 features. Alternatively, species such as dicarbon monoxide (C_2O), a free radical formed via irradiation of carbon suboxide (C_3O_2) and CO ices at cryogenic temperatures express features centered near 5.02 μm (e.g., M. E. Jacox et al. 1965; C. J. Bennett et al. 2010b).

Similar to the TP and BP + P modes, the 3.33 μm band is only observed in environments dominated by crystalline CO_2 ice, such as CO_2 frost clouds on Mars (e.g., J. F. Bell et al. 1996). The vibrational modes that contribute to this band in solid-state CO_2 are not well characterized. However, an ~3.3 μm feature observed in experiments involving CO_2 gas has been attributed to a $\nu_2 + \nu_3$ "electric-dipole-forbidden" transition mode that can gain intensity from a magnetic dipole transition arising from vibrational angular momentum (M1; K. Kazakov & A. Vigasin 2021). Future analytical work, and perhaps additional experiments, are required to determine the modes contributing to the 3.33 μm feature expressed by CO_2 ice.

Comparison to substrates mantled by CO_2 ice and CO_2:H_2O mixtures. Ground-based observations indicate that the spectral properties of the large Uranian moons are consistent with H_2O ice well mixed with dark and reddish material(s), capped by isolated deposits of crystalline CO_2 ice that likely include minor amounts of other carbon oxides (e.g., W. Grundy et al. 2006; R. J. Cartwright et al. 2022). To better understand the spectral properties of CO_2 mantling these moons' regoliths, we compared the G395M data of Ariel's trailing hemisphere to laboratory spectra of stratified and textured layers, including an ~10 μm thick layer of CO_2 ice condensed onto an ~1 μm thick, proton-irradiated organic residue, and an ~15 μm thick layer of CO_2 ice condensed directly onto the Infragold

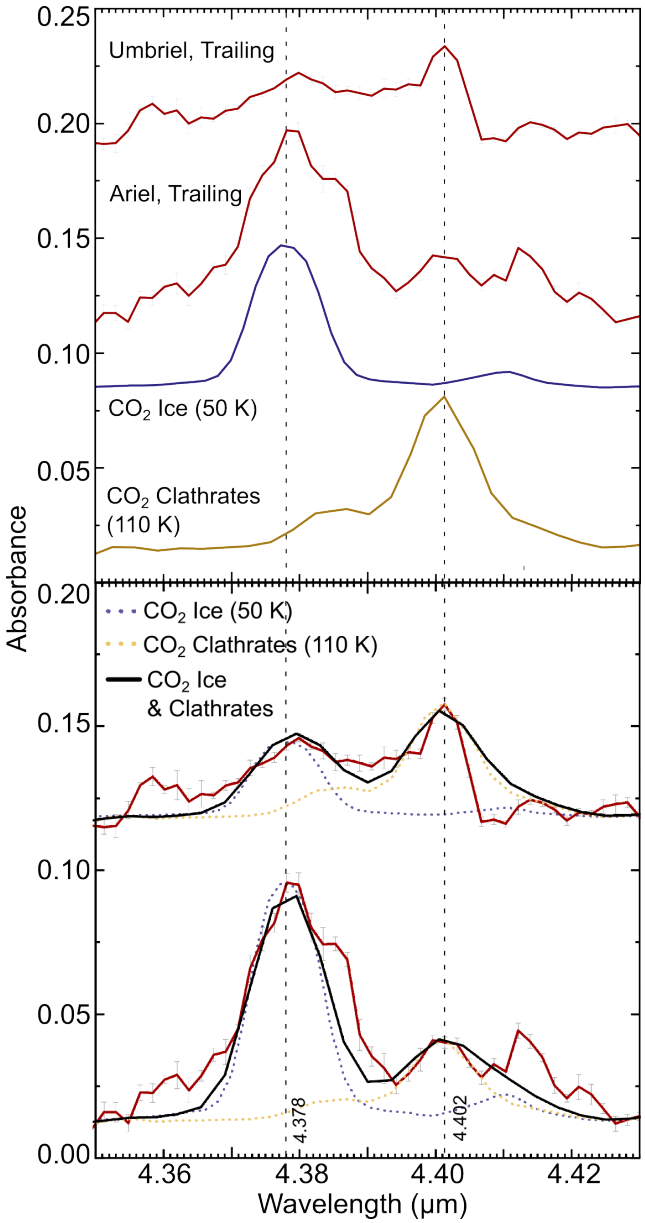

Figure 8. Top: absorbance spectra (–log(reflectance)) of CO_2 ice (50 K) measured using INGMAR (e.g., E. Hénault et al. 2025) and CO_2 clathrates (110 K; A. Oancea et al. 2012). These laboratory spectra are compared to G395M reflectance data of Ariel trailing and Umbriel trailing, converted to absorbance (–log(reflectance)) and offset vertically for clarity. Bottom: scaled versions of the CO_2 ice and CO_2 clathrates spectra, and linear combinations of these two laboratory spectra, fit to the G395M data, offset vertically for clarity. These scaled spectra of CO_2 ice and CO_2 clathrates provide reasonable matches to the 4.38 and 4.4 μm features, respectively. Additional features near 4.36 and 4.41 μm are not well matched by these laboratory species. These scaled spectral data offer useful but nonunique solutions, and other scaled combinations warrant study in future work.

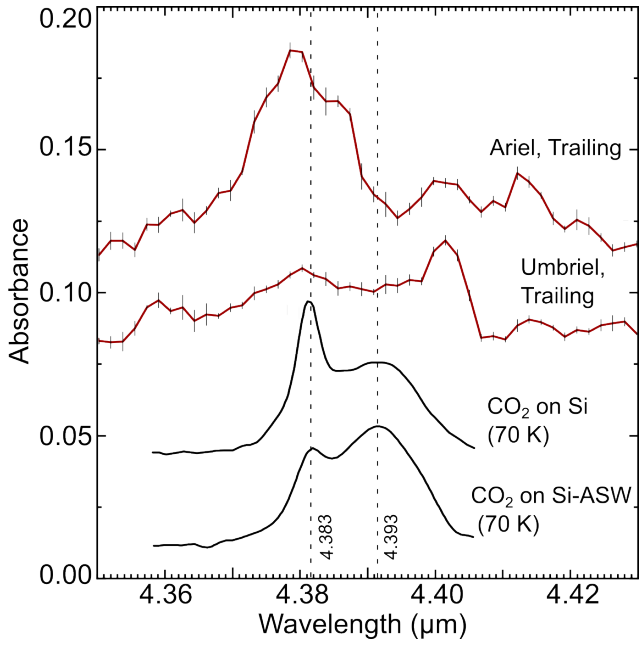

Figure 9. Laboratory spectra (modified from T. Suhasaria et al. 2025) of CO_2 ice condensed on a silicate-rich, meteorite simulant layer (70 K) and amorphous H_2O ice ("ASW") deposited on a meteorite simulant layer (70 K). These laboratory spectra are compared to G395M reflectance data of Ariel trailing and Umbriel trailing, converted to absorbance (–log(reflectance)) and offset vertically for clarity. Dashed lines highlight spectral features identified in the laboratory data near 4.383 and 4.393 μm. The 4.383 μm peak is offset from the Ariel and Umbriel data, but the 4.393 μm peak provides a potentially useful match to Umbriel's broad $^{13}CO_2$ feature that warrants study in future work.

substrate (Figure 6). The laboratory spectra show a prominent, double-lobed scattering peak, with wavelength positions consistent with Ariel's double-lobed scattering peaks, centered near 4.20 and 4.25 μm, demonstrating that layering and surface roughness can enhance CO_2 scattering peaks. Although the overall shape and intensity of Ariel's peaks are not well matched by the laboratory data, they demonstrate that CO_2 ice veneers capping rough(er) substrates can crudely replicate the scattering peaks. Similarly, synthetic spectra of granular CO_2 ice (10 μm diameter grains; optical constants reported in P. A. Gerakines & R. L. Hudson 2020), are also able to crudely match Ariel's 4.20 and 4.25 μm peaks (R. J. Cartwright et al. 2024a), highlighting the importance of scattering between grains in a regolith for reproducing these features.

The laboratory spectrum also shows features centered near 4.38, 4.40, 4.41, and 4.46 μm, with central wavelengths well aligned with features in the Ariel spectrum, suggesting that relatively pure CO_2 ice might explain much of the spectral structure observed in the G395M data. Indeed, earlier laboratory experiments showed that thick CO_2 ice substrates can express notable features at these wavelengths (see Figure 2 in D. A. Dows & V. Schettino 1973). Comparing Ariel's 4.27 μm feature to the laboratory data, however, reveals a notable disparity, with the CO_2 ν_3 mode shifted to 4.29 μm in the laboratory spectrum. Similarly, a prominent ~4.07 μm "absorption" feature in the laboratory data is not observed in the Ariel data. This 4.07 μm feature has been attributed to a Christiansen effect in CO_2 ice (M. N. De Prá et al. 2025), where the real index n approaches unity, leading to reduced internal scattering and lower reflectance, thereby mimicking absorption, even at wavelengths where the extinction coefficient, k, is small (B. Hapke 2012). However, this feature is significantly weakened in samples where CO_2 is embedded in other materials with higher refractive indices (M. N. De Prá et al. 2025). The absence of this 4.07 μm feature therefore hints that some fraction of CO_2 on the Uranian moons is well mixed or perhaps trapped in another compound like H_2O ice, hypothetically supporting the presence of CO_2 clathrates.

Potential band splitting in $^{13}CO_2$ ice. Between 4.36 and 4.42 μm, the G395M data collected over Ariel's and Umbriel's

trailing hemispheres exhibit a multilobe structure that has been observed previously in thick CO_2 ice deposits (as shown in Figure 2 of D. A. Dows & V. Schettino 1973), as well as CO_2 ice mixed with CO_2 clathrates (E. Dartois & B. Schmitt 2009; A. Oancea et al. 2012). Other studies have revealed multilobe structure in $^{13}CO_2$ features between 4.36 and 4.40 μm in dense clouds enveloping young stars observed by JWST/NIRSpec, possibly resulting from CO_2 mixed with H_2O ice and/or CH_3OH (e.g., N. G. Brunken et al. 2024), demonstrating that band splitting of CO_2 features can occur in astrophysical environments. Here, we investigate possible band splitting in the $^{13}CO_2$ features identified in G395M reflectance data of Ariel and Umbriel by first converting these spectra to absorbance (–log(reflectance)). We then subtracted off the continua between 4.3 and 4.5 μm, and compared the resulting continua-subtracted G395M data to laboratory data of CO_2 cocondensed with H_2O ice, CO_2 condensed onto a thin organic residue, CO_2 condensed on an amorphous $MgFeSiO_4$ meteorite simulant, and a linear mixture of a CO_2 ice spectrum combined with a CO_2 clathrate spectrum (Figures 7, 8, and 9). The rest of this section focuses on our analysis of these absorbance-converted G395M data of Ariel and Umbriel. This analysis is provided as a starting point to motivate future studies that more rigorously investigate the nature of CO_2 on the Uranian moons.

The laboratory spectrum of CO_2 condensed on an organic residue (warmed to 90 K), expresses additional structure between 4.40 and 4.43 μm, that approximates the central wavelengths of Ariel's 4.40 and 4.41 μm features (Figure 7). This laboratory spectrum also exhibits a broad absorption band between 4.43 and 4.48 μm that is comparable to the wavelength range of Ariel's 4.47 μm feature. Similar components may contribute to the spectral structure observed in the G395M data of Umbriel near 4.4 μm, although the Umbriel data do not display 4.41 and 4.47 μm features, making the match less compelling than for Ariel. The laboratory spectra of CO_2 cocondensed with H_2O ice does not express a multilobe morphology and has a notably broader 4.38 μm feature, stretching between ~4.37 and 4.40 μm, representing a poorer match to the narrower features expressed by the G395M data of both Ariel and Umbriel (Figure 7). An additional 4.36 μm sideband expressed by the G395M data of these two moons (labeled with a "?" in Figure 7) is not observed in any of the laboratory data we analyzed. Determining whether the 4.36 μm feature results from an unidentified compound or combination of compounds is left for future work.

Next, we compared the G395M data to a linear mixture of CO_2 ice (50 K) condensed onto an organic residue and CO_2 clathrates (110 K; A. Oancea et al. 2012), scaled to the Ariel spectrum (0.075 and 0.59, respectively) and Umbriel spectrum (0.026 and 0.85, respectively). This comparison shows that these two components can approximate the shape of the multilobe structure expressed by these moons, except for the previously mentioned 4.36 μm side bands (Figure 8). These scaled laboratory spectra provide a nonunique solution and other scaled combinations may provide reasonable matches. Nonetheless, this comparison shows that mixtures of CO_2 ice and CO_2 clathrates can provide reasonable matches to the spectral properties of these moons. The laboratory spectra of CO_2 condensed on a layer of amorphous $MgFeSiO_4$, and the same amorphous silicate layer capped by an additional layer of amorphous H_2O ice (T. Suhasaria et al. 2025), exhibit double-lobed $^{13}CO_2$ features, centered near 4.383 and 4.393 μm (Figure 9). The laboratory spectra do not exhibit 4.41 μm features, unlike the Ariel G395M data. However, the silicate–CO_2 stratified substrates show a band of absorption between 4.37 and 4.40 μm, appearing to provide a useful match to the G395M data of Umbriel, which exhibit a stronger absorption profile near 4.39 μm compared to Ariel.

These comparisons highlight that the finer scale structure of Ariel's $^{13}CO_2$ ν_3 mode is reasonably approximated by CO_2 ice (90 K) condensed on an irradiated organic residue, which may also contribute to its broad 4.47 μm feature. In this scenario, Ariel's 4.41 μm feature could include contributions from $^{13}C^{16}O^{18}O$ (M. Loeffler et al. 2005; C. J. Bennett et al. 2010b). Additionally, Ariel's broad 4.47 μm feature (spanning ~4.44 to 4.49 μm) could include contributions from $^{13}C^{18}O_2$ near 4.45 μm (M. Loeffler et al. 2005). The relative strength of Ariel's 4.47 μm band compared to the laboratory data (Figure 7) suggests that other, non-CO_2 compounds may contribute as well, such as carbon-chain oxides and nitriles. CO_2 ice (50 K) mixed with CO_2 clathrates (110 K) can also reproduce the multilobe structure expressed in the G395M data of Ariel and Umbriel between 4.36 and 4.42 μm. The structure of Umbriel's $^{13}CO_2$ ν_3 mode is not well matched by any one of the laboratory spectra inspected here, but could be better matched by a combination of different laboratory spectra, including CO_2 cocondensed with H_2O or CO_2 condensed on amorphous silicates.

Does CO_2 contribute to the 4.02 μm band? Similar to the measurements of CO_2 and CO reported here, the 4.02 μm feature (secure detection; Table 2) is strongest on Ariel, in particular on its trailing hemisphere. However, the next strongest 4.02 μm bands are on Titania, followed by Oberon, and the weakest 4.02 μm bands are on Umbriel, unlike the trends in CO_2 and CO (Table 3), indicating that this feature could result from other species. Furthermore, none of the CO_2-dominated laboratory spectra presented here, or synthetic spectra of CO_2 ice presented previously (R. J. Cartwright et al. 2024a), show features consistent with the 4.02 μm band. Although the continuum of H_2O ice exhibits a pronounced slope change in this wavelength region that could hypothetically contribute to the 4.02 μm band, the strongest H_2O and HDO ice features we measured are on Titania, not Ariel, inconsistent with the reported 4.02 μm band strengths.

It therefore seems more likely that another component dominates contributions to this feature, such as carbonate minerals, as suggested by a prior study (R. J. Cartwright et al. 2024a). To investigate this possibility further, we compared continuum-divided 4.02 μm bands of Ariel and Titania to continuum-divided 4 μm features exhibited by laboratory spectra of anhydrous sodium carbonate (Na_2CO_3) and calcium carbonate ($CaCO_3$), as well as a 4 μm feature expressed by Jupiter's moon Callisto (Figure 10), which has been attributed to carbonates (R. Johnson et al. 2004; R. J. Cartwright et al. 2024b). The laboratory spectra of carbonates and Callisto's 4 μm feature share similar central wavelengths and morphologies to the 4.02 μm band on the Uranian moons, providing another piece of evidence supporting the presence of carbonates. Of note, we see no evidence for a 3.5 μm band complex associated with carbonates (R. Hexter 1958), possibly because it fully overlaps the long-wavelength wing of the broad 3 μm H_2O ice band (e.g., R. Mastrapa et al. 2009).

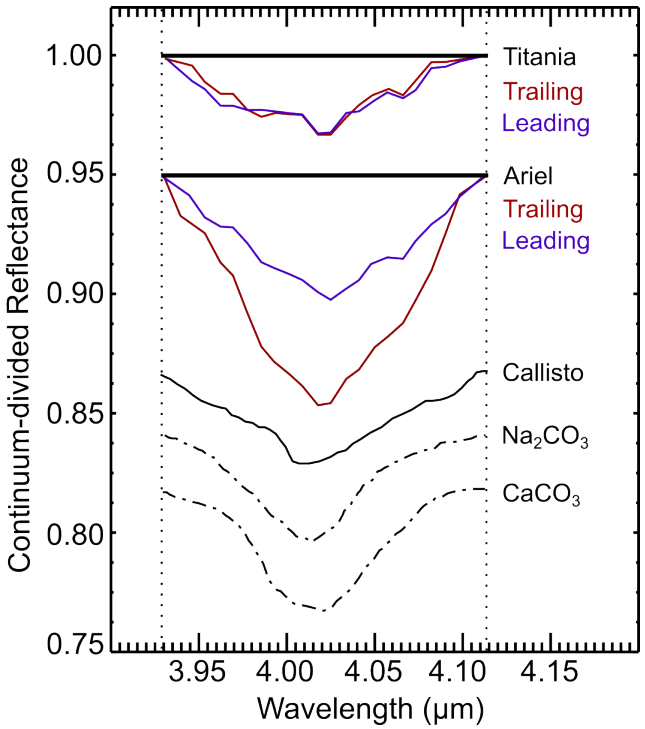

Figure 10. Continuum-divided reflectance data showing 4 μm bands identified in the leading and trailing hemisphere data collected at Ariel and Titania (secure detections; Table 2), IRTF/SpeX data of Callisto's leading hemisphere (originally reported in R. J. Cartwright et al. 2020b), and laboratory data of anhydrous sodium carbonate and calcium carbonate (R. A. Nyquist et al. 1997), with uncertainties removed and offset vertically for clarity. The 4 μm features identified in the G395M data and reported in Table 3 (3.96–4.11 μm) are slightly narrower than the feature identified on Callisto (3.92–4.11 μm). Consequently, we remeasured the 4 μm features in the G395M data of Titania and Ariel using the same wavelength range as Callisto's 4 μm band, thereby enabling a more suitable comparison between these three moons.

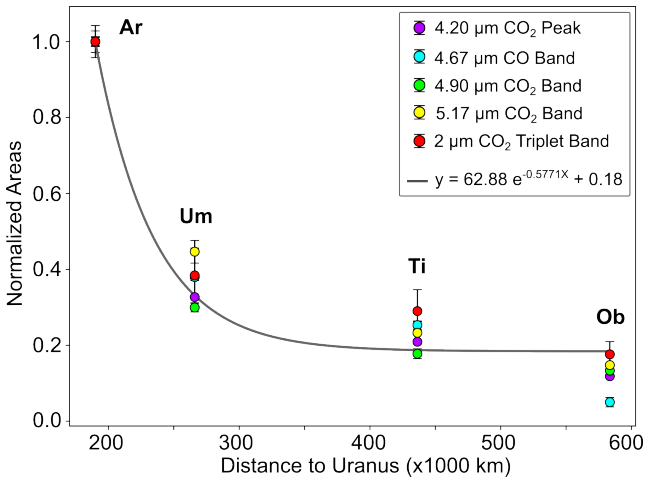

Figure 11. Areas and approximate 1σ uncertainties for the 4.20, 4.67, 4.90, and 5.17 μm spectral features, measured by JWST/NIRSpec, and the CO_2 triplet band, measured by IRTF/SpeX, for the trailing hemispheres of Ariel ("Ar"), Umbriel ("Um"), Titania ("Ti"), and Oberon ("Ob"), normalized to Ariel. These normalized measurements use the same colors as the corresponding measurements shown in Figure 4. A global, nonunique model (offset exponential) has been fit to the data to visually illustrate the comparable trends for each of these features as a function of distance from Uranus. The overall trend in band and peak areas demonstrates that CO_2 and CO are concentrated on the trailing hemispheres of the inner moons, possibly more consistent with a charged particle irradiation origin and less so localized geologic exposure of CO_2 on each moon.

Alternatively, the 4.02 μm band could result from a 4.07 μm feature in CO_2 ice (marked with an "×" in Figure 6), generally attributed to a Christiansen effect where the real part of the refractive index for CO_2 drops below unity, reducing internal scattering and limiting reflectance, thereby mimicking the spectral profile of a strong absorption band (e.g., M. N. De Prá et al. 2025). In this scenario, some currently unidentified process would have to account for the notable difference between the position of this purported Christiansen feature and the 4.02 μm band (~0.05 μm wavelength shift). On balance, carbonate minerals are the most useful match in terms of central wavelength and band morphology, and we favor this interpretation for the origin of the 4 μm feature on the Uranian moons (Table 2). Future laboratory experiments involving crystalline CO_2 ice and other carbon oxides under conditions relevant to the Uranus system are likely needed to determine whether carbonates or some other combination of species can replicate the morphology of the 4.02 μm band.

4. Discussion

4.1. Distribution and Spectral Signature of CO_2

The measurements (Tables 3, 4, and 5) and analyses (Figures 4 and 11) reported here demonstrate that most of the spectral features associated with CO_2 and CO (~2.9–5.3 μm) are stronger on the trailing hemispheres of all four moons and decrease in strength with increasing distance from Uranus (Figure 11). These results are consistent with the hemispherical and radial trends measured in ground-based reflectance data for the CO_2 triplet band (shown here in Figure 4(e); W. Grundy et al. 2003, 2006; R. J. Cartwright et al. 2015).

Unlike prior ground-based observations, however, the G395M data for the leading hemispheres of these moons also exhibit CO_2 features, in particular a strong absorption band centered near 4.27 μm, resulting from the ν_3 TO mode of $^{12}CO_2$ ice. Indeed, the band area measurements reported here indicate that the 4.27 μm feature is stronger on the leading hemispheres of these moons compared to their trailing sides, unlike all other measurements of carbon oxides. Curiously, when comparing the four moons, Umbriel's leading hemisphere exhibits the strongest 4.27 μm band, unlike all other CO_2-related features that are significantly stronger on Ariel's trailing side, in both ground-based and JWST/NIRSpec datasets (Figure 4). Additionally, all other measured CO_2 and CO features on Umbriel's leading hemisphere are weaker than those on its trailing side and weaker than those on the leading and trailing hemisphere of Ariel.

A plausible explanation for these apparent oddities is that the 4.20 μm scattering peaks observed on the trailing hemispheres of these moons, and Ariel's leading hemisphere, partially "fill in" the adjacent 4.27 μm band, spuriously making these features appear weaker. Possible evidence for such a fill-in effect can be seen in the trailing/leading spectral ratios, which exhibit large peaks at both 4.2 and 4.27 μm for all four moons (Figure 3). Photon penetration depths are extremely small in the wavelength range of the ν_3 mode of $^{12}CO_2$ (see Figure 4 in R. J. Cartwright et al. 2024a), and light effectively interacts with only the outer surfaces of CO_2 ice grains. Using the 4.27 μm feature to diagnose the spectral properties of CO_2 ice is therefore challenging, and we caution the reader from drawing strong conclusions from the 4.27 μm

band strength trends reported here. We instead suggest that the spectral properties of weaker combination and overtone modes, outside the wavelength range of the strong ν_3 mode for $^{12}CO_2$ (~4.2–4.3 μm), may provide more utility for understanding the spatial distribution and vertical stratification of CO_2 ice on the large Uranian moons, and perhaps other astrophysical environments that are enriched with crystalline CO_2 ice layers.

As seen by JWST, the Uranian moons are point sources and all of the collected G395M data are disk integrated. Because of the obliquity of the Uranus system (subsolar latitude ~ 64° at the time of the GO 1786 observations), the moons' observable disks included a fraction of their trailing hemispheres during the leading hemisphere observations and vice versa. Consequently, it is feasible that CO_2 located in deposits on their trailing hemispheres may contaminate the leading hemisphere observations reported here. Such "cross-hemispherical" contamination could hypothetically explain why CO_2 has yet to be confirmed on the leading hemispheres of these moons in ground-based data (W. Grundy et al. 2003, 2006; R. J. Cartwright et al. 2015), which were mostly collected in late southern summer and early northern spring at Uranus (30°S–30°N), when cross-hemispherical contamination between their leading and trailing sides was negligible. To investigate this possibility, we calculated the fraction of cross-hemispherical contributions for each GO 1786 observation (using a disk-area calculation provided in B. Holler et al. 2016), finding only ~26.7% overlap in these moons' disk areas, with most of this overlap (~18.7%) limited to subsolar latitudes > 45°N, where CO_2 is predicted to be strongly depleted if not entirely absent (W. Grundy et al. 2006; M. M. Sori et al. 2017; J. K. Steckloff et al. 2022; S. M. Menten et al. 2024).

It is therefore feasible that the CO_2 detected in GO 1786 observations collected over the leading hemispheres of these moons results from deposits physically located on their leading hemispheres and spatially distinct from CO_2 on their trailing sides. Consequently, the results reported here further highlight the ubiquity of CO_2 across the Uranus system. It is possible, however, that CO_2 ice deposits located on the leading hemispheres of the moons were initially exposed, or radiolytically formed, on their trailing sides, before migrating in response to ongoing seasonal sublimation–condensation cycles. Indeed, a global layer of CO_2 at least a few millimeters thick may migrate across the surfaces of Uranus' large moons each Uranian year (J. K. Steckloff et al. 2022), which would provide sufficient amounts of CO_2 to explain the detected spectral signature of this molecule on their leading hemispheres.

4.2. CO_2 Frost Layer(s) Mantling the Regoliths of the Uranian Moons?

Prior work indicates that exposed CO_2 layers are at least a few millimeters thick on Ariel's trailing hemisphere, possibly $\gtrsim$10 mm thick (see Figure 4 in R. J. Cartwright et al. 2024a). Based on existing laboratory data of thick CO_2 ice deposits, we expected to find near-saturated ν_3 modes between 4.2 and 4.3 μm (G. B. Hansen 1997; E. Quirico & B. Schmitt 1997a, 1997b). For example, Neptune's moon Triton, which shows a wealth of weaker CO_2 ice combination and overtone modes (e.g., D. P. Cruikshank et al. 1993; W. Grundy et al. 2010; B. Holler et al. 2016), also exhibits near total absorption between ~4.2 and 4.3 μm (I. Wong et al. 2025), consistent with the strong ν_3 mode of CO_2, with likely contributions from an 4.25 μm N≡N stretching mode exhibited by N_2 ice (e.g., D. DiLella & D. Tevault 1986). In contrast, this wavelength range is characterized by prominent scattering peaks (~4.16–4.24 μm) and relatively weak absorption bands (~4.24 and 4.30 μm) on the trailing hemispheres of the large Uranian moons, as discussed in Section 4.1. Based on the laboratory data presented here, CO_2 ice veneers can express large scattering peaks when condensed onto rough surfaces, as seen in our spectra of CO_2 condensed onto organic residues and onto Infragold substrates (Figure 6). Conversely, CO_2 ice deposits on Triton may instead be dominated by geologically thick outcrops of exposed "bed ice" (B. Holler et al. 2016), which strongly absorbs light. A possibly more relevant spectral analog for the Uranian moons may be found at Mars, where transient CO_2 frost clouds express prominent scattering peaks between 4.2 and 4.3 μm (e.g., K. C. Herr & G. C. Pimentel 1970; F. Montmessin et al. 2007; T. Mangan et al. 2017; S. Aoki et al. 2018), as well as a host of other CO_2 features, including a prominent 3.33 μm band (J. F. Bell et al. 1996).

Inspired by CO_2 frost clouds at Mars, we offer the following "working model" that may be able to explain the observed spectral properties of CO_2 on the Uranian moons. Perhaps the surfaces of the Uranian moons are coated by a highly porous veneer of CO_2 frost (perhaps 1–10 μm thick), capping a more compacted layer of CO_2 ice, mixed with CO_2 clathrates and possibly other carbon oxides (a few to tens of millimeters thick). These CO_2-dominated layers mantle H_2O ice and dark regolith materials, possibly consistent with the low to moderate albedos and gray-toned surfaces imaged by V2 at each of these moons (e.g., B. A. Smith et al. 1986; P. Helfenstein et al. 1989, 1991; B. J. Buratti & J. A. Mosher 1991). Such a layering of CO_2 could be transient, especially the exposed CO_2 frost veneer, migrating in response to subsolar heating, as predicted by volatile transport models (W. Grundy et al. 2006; M. M. Sori et al. 2017; J. K. Steckloff et al. 2022; S. M. Menten et al. 2024). The seasonal migration–condensation cycling of CO_2 might continually refresh its spectral properties and likely help preserve the hypothesized high-porosity veneer, which in turn could enhance scattering and contribute to the prominent 4.2 μm scattering peaks observed by JWST/NIRSpec.

Supporting this scenario, ground-based visible wavelength polarimetry data suggest that the large Uranian moons are mantled by a highly porous (~95%), crumbly layer of fine-grained material (~1 μm diameters) of unknown composition (V. Afanasiev et al. 2014). Radiative transfer modeling of ground-based NIR observations also support the presence of small grains mantling the Uranian moons (R. J. Cartwright et al. 2020a), and suggest that at least two CO_2 ice grain sizes (1–10 and ~50 μm) are required to match the morphologies of the CO_2 triplet bands (R. J. Cartwright et al. 2015, 2022). Furthermore, Titania's H_2O ice features are stronger than Ariel's H_2O ice features in the G395M data (Table 5), but in ground-based datasets, Ariel exhibits stronger H_2O ice features than the other large Uranian moons. This disparity likely results from differences in photon penetration depths into H_2O ice, with light penetrating to greater depths at NIR wavelengths probed from the ground (~0.8–2.5 μm; ~0.05–10 mm depths) compared to the wavelength range of the G395M (~2.9–5.3 μm; ~0.001–0.05 mm depths). Consequently, shorter-wavelength spectra could be better sampling Ariel's

regolith underlying an exposed CO_2 ice veneer, thereby contributing to Ariel's stronger H_2O ice spectral features in ground-based datasets compared to the G395M data, where relatively CO_2-poor Titania expresses stronger H_2O ice features.

Therefore, the combination of scattering peaks and relatively weaker overtone and combination modes for CO_2 ice, and the disparities in the spectral signature of H_2O ice in different wavelength ranges, are potentially consistent with our working model involving two stratified layers of CO_2 ice. This model assumes that there is an exposed veneer of small grains that promotes scattering, with a layer of larger CO_2 ice grains, and perhaps CO_2 clathrates with minor amounts of other carbon oxides, beneath, which dominates contributions to weaker combination and overtone modes. Both CO_2-dominated layers may be partially transient, migrating in response to subsolar heating, especially from the constantly sunlit summer poles, promoting the growth of long-term cold traps at low latitudes, where diurnal heating variations dampen sublimation rates.

4.3. Sources of CO_2 on the Uranian Moons

Radiolytic production cycle? Since the discovery of the CO_2 triplet band on Ariel, Umbriel, Titania, and Oberon, the best supported hypothesis to explain the distribution and origin of this molecule has been charged particle bombardment of preexisting carbon-rich components mixed with H_2O ice in the regoliths of these moons, primarily on their trailing hemispheres, generating radiolytic CO_2 (W. Grundy et al. 2003, 2006; R. J. Cartwright et al. 2015). In this scenario, CO_2 molecules are generated primarily at high latitudes, and then they migrate in response to subsolar heating to long-term cold traps, located primarily at low latitudes. Additionally, CO would also be radiolytically generated, primarily from continued radiation processing of the newly formed CO_2 molecules. Such a combination of continual radiolytic production, seasonal volatile migration, and long-term sequestration of CO_2 (and perhaps CO) in cold traps could therefore explain how equatorial deposits of CO_2 ice gradually grow and remain quasi stable over long timescales (M. M. Sori et al. 2017; R. J. Cartwright et al. 2022; S. M. Menten et al. 2024).

At first glance, the nondetection of the CO_2 triplet band on the innermost large moon Miranda (J. M. Bauer et al. 2002; F. Gourgeot et al. 2014; R. J. Cartwright et al. 2018; R. A. DeColibus et al. 2022, 2023), which is deeply embedded in Uranus' magnetosphere, appears difficult to reconcile with a primarily radiolytic origin for CO_2. However, the considerably lower gravity of Miranda makes volatile loss via escape to space more effective compared to the larger moons. Indeed, thermodynamical models predict that ~50% of migrating CO_2 molecules escape Miranda's surface before completing even one suborbital ballistic hop (M. M. Sori et al. 2017). As a result, the escape rate of CO_2 may outpace its radiolytic production rate on Miranda, thereby preventing the buildup of thick deposits that can express CO_2 triplet bands.

As part of a different study, JWST/NIRSpec revealed the ν_3 mode of solid-state CO_2 on Miranda, as well as in Uranus' rings and ring moons and on its far-flung irregular satellites (M. Belyakov & M. Brown 2024; M. Belyakov 2025). When viewed in context with existing data of the largest moons, solid-state CO_2 is apparently widespread throughout the Uranian system. Uranus' rings also show hints of other features that could result from carbon-bearing compounds (M. Belyakov & M. Brown 2024; M. Belyakov 2025). If these C-bearing constituents are present and mixed with H_2O ice, they may represent additional radiolytic products and/or some of the raw materials from which radiolytic CO_2 is being generated via interactions with Uranus' magnetosphere. Indeed, the G395M data of Ariel exhibit subtle features near 3.9 and between 5 and 5.1 μm (Figure 3), possibly resulting from H_2CO_3 (e.g., M. Moore & R. Khanna 1991) and the free radical C_2O (e.g., C. J. Bennett et al. 2010b), respectively, which if present would be short-lived (especially C_2O) and likely diagnostic of ongoing radiation processing of Ariel's surface. Such moon–magnetosphere interactions would sputter CO_2 and other carbon oxides off Ariel's surface, possibly contributing to an uncharacterized source of plasma detected near the moon's location in Uranus' magnetosphere (I. J. Cohen et al. 2023), with CO_2 escaping from Miranda potentially also contributing to this plasma.

Native constituent? The spectral properties of CO_2 on Uranus' largest moons are largely consistent with crystalline CO_2 ice, exhibiting numerous subtle features only observed in thick layers of pure CO_2 ice (e.g., G. B. Hansen 1997; E. Quirico & B. Schmitt 1997a, 1997b). These subtle CO_2 features are not present in Uranus' rings and ring moons or its irregular satellites, hinting that at least some of the CO_2 on the large moons has an alternative source. In this scenario, CO_2 ice deposits may build up from passive outgassing, especially at the frigid temperatures of their winter poles (20–30 K; M. M. Sori et al. 2017) where even hypervolatile CO should condense. Such outgassing could be dominated by diffuse emissions from the interiors of these moons and not dramatic geyser eruptions. CO_2 clathrates may also be present and contribute to the multilobe structure of the ν_3 mode of $^{13}CO_2$ (Figure 8). Clathrate hydrates often form in high-pressure environments, such as on Earth's seafloors, and if present on the Uranian moons, they could point to an internal origin for CO_2 (R. J. Cartwright et al. 2024a). Clathrates can, however, form at low temperatures (10 K) and pressures ($\sim 10^{-10}$ mbar) consistent with conditions in the ISM (J. Ghosh et al. 2023). By extension, perhaps clathrates might form on the airless surfaces of the Uranian moons, although forming them in this manner would still require sufficiently long timescales to enable CO_2–H_2O interaction and cocondensation to make thermodynamically stable phases. Additionally, the results reported here are consistent with prior spectral analyses that suggested internally derived carbonate minerals could be present on Uranus' moons (R. J. Cartwright et al. 2023, 2024a).

Although we speculate that weak 3.9 μm and 5.02 μm features in the G395M data may result from the common radiolytic products H_2CO_3 and C_2O, respectively, these subtle bands could instead result from weak and unattributed CO_2 features, expressed by thick, crystalline ice-dominated deposits (see Figure 5 for an example of such an unattributed feature). Furthermore, we found no evidence for another established radiolytic product, H_2O_2, on Ariel or the other moons. H_2O_2 has been detected on the icy Galilean moons Europa and Ganymede and Pluto's moon Charon, primarily attributed to moon–magnetosphere interactions at Jupiter (e.g., R. Carlson et al. 1999; S. K. Trumbo et al. 2023) and solar ultraviolet and interplanetary medium Lyα photons, solar wind, and Galactic cosmic rays at Charon (S. Protopapa et al. 2024). Another

study, reporting optical wavelength spectra of Ariel, Umbriel, Titania, and Oberon, found no evidence for spectral features consistent with trapped O_2 near 577 and 625 nm (R. A. DeColibus et al. 2026), which is a telltale constituent for ongoing radiolytic processing of the icy Galilean moons' surfaces (e.g., W. M. Calvin et al. 1996; R. Johnson & W. Jesser 1997; J. R. Spencer & W. M. Calvin 2002; A. V. Oza et al. 2026). Unlike Saturn's midsized, inner moons (A. R. Hendrix et al. 2018), the inner Uranian moons Ariel and Umbriel show no evidence for preferential radiation darkening of their trailing hemispheres at ultraviolet and visible wavelengths (C. Soto et al. 2025), further supporting a scenario where radiation processing is not a dominant chemical process at these moons. Of note, the spectral signatures of H_2O_2 and other presumed H_2O–CO_2 irradiation products detected on Jupiter's moons are much weaker or entirely absent from the surfaces of Saturn's icy moons, indicating that the spectral signature of radiolysis is likely subtler on icy bodies outside of the intense Jovian magnetosphere.

Both native and radiolytic in origin? On balance, it seems plausible that solid-state CO_2 in the Uranus system has multiple sources, including radiolytic production and geologic exposure and emplacement of native CO_2 ice and clathrates, possibly mixed with other compounds that are hypothesized to be present and internally derived, such as carbonates (R. J. Cartwright et al. 2023, 2024a) and NH_3- and NH_4-bearing species (J. M. Bauer et al. 2002; R. J. Cartwright et al. 2018, 2020c, 2023; R. A. DeColibus et al. 2023). Potentially analogous to this dual origin scenario for CO_2 on Uranus' moons, the spectral properties of CO_2 observed on the warmer surfaces of the Galilean satellites have also been interpreted to support both radiolytic and endogenic origins. Data returned by the Near Infrared Mapping Spectrometer on the Galileo spacecraft measured $^{12}CO_2$ ν_3 features with central wavelengths shifted to 4.25–4.26 μm on Europa, Ganymede, and Callisto, consistent with radiolytically produced CO_2 that is trapped or "complexed" within hydrated salts and/or organic residues mixed with H_2O-bearing minerals in which it is generated (e.g., T. McCord et al. 1997, 1998b; R. J. Cartwright et al. 2024b). Conversely, the observed spatial association between CO_2 and geologic features like craters on Callisto has been attributed to native CO_2, exposed by impact events (C. Hibbitts et al. 2000, 2002). Similarly, analyses of JWST/NIRSpec data of Europa suggest that some of the CO_2 on its surface is likely derived from its interior and exposed in chaos-dominated regions like Tara and Powys regiones (S. K. Trumbo & M. E. Brown 2023; G. Villanueva et al. 2023; R. J. Cartwright et al. 2025).

Reflectance spectra collected over Europa's Tara and Powys regiones also exhibit 3.505 μm features, attributed to H_2O_2 formed via irradiation of H_2O ice (e.g., R. Carlson et al. 1999). Laboratory experiments have demonstrated that the presence of a minor amount of CO_2 mixed with H_2O can enhance the formation of H_2O_2 (B. D. Mamo et al. 2025), highlighting the chemical interplay between endogenically derived CO_2, H_2O, and charged particles within the Jovian magnetosphere at Europa. Although we find no compelling evidence for H_2O_2 on the Uranian moons, it is possible that a cap of seasonally mobile CO_2 effectively absorbs trapped charged particles, thereby shielding underlying H_2O ice from interactions with Uranus' magnetosphere and stymieing H_2O_2 production. If such a cap exists (described above in Section 4.2), charged particle sputtering of CO_2 from this layer could be significant (U. Raut & R. Baragiola 2013), hypothetically contributing to predicted, but yet to be detected, exospheres at Ariel and the other moons (e.g., J. K. Steckloff et al. 2022; U. Raut et al. 2025). Furthermore, the possible presence of carbonates supports endogenically derived carbon oxides on these moons, which could feasibly include outgassed CO_2, as hypothesized for Europa (S. K. Trumbo & M. E. Brown 2023), and would imply formation in the presence of liquid water (e.g., F. G. Carrozzo et al. 2018). Carbonates could have formed in the interiors of the Uranian moons from interactions between melted H_2O ice and dissolved CO_2, mixed with silicate minerals (C. R. Glein & J. H. Waite 2020). If CO_2 was accreted by these moons, its presence would mean that temperatures in the circum-Uranian disk (or subnebula) were below the condensation temperature of CO_2 ice when they formed (a representative upper limit is $\sim$80 K; O. Mousis et al. 2009). Of note, dust-delivered carbonate grains from Jupiter's irregular satellites might also contribute to Callisto's 4 μm band (R. J. Cartwright et al. 2024b; B. N. Sharkey et al. 2025), complicating a solely endogenic origin story for CO_3-bearing species.

Unraveling whether the primary source of CO_2 is in situ production via radiation processing of regolith materials or passive outgassing and geologic exposure on the large moons is challenging using JWST and similar standoff platforms. Measurements made by instruments on an orbiter would vastly expand our knowledge of these carbon-oxide-rich moons and the origin and fate of CO_2 across the broader Uranus system. In particular, an NIR mapping spectrometer, dust analyzer, and ion and neutral mass spectrometer would be an ideal combination of instruments for constraining possible subsurface–surface–exosphere exchange of carbon oxides at Ariel and the other Uranian moons (R. Cartwright et al. 2021). A similar combination of instruments will be leveraged by the Europa Clipper spacecraft to understand material cycling on Europa (T. Becker et al. 2024).

5. Summary and Conclusions

We analyzed JWST/NIRSpec reflectance spectra collected over the leading and trailing hemispheres of Ariel, Umbriel, Titania, and Oberon, revealing prominent CO_2 ice and CO ice absorption features and scattering peaks, in particular on the inner moons, Ariel and Umbriel (Figures 1 and 2). We detected a suite of other spectral features that have previously been suggested to result from CO_2 clathrate hydrates, carbonates, carbon-chain oxides, and nitriles (R. J. Cartwright et al. 2024a). Through comparison to laboratory data of CO_2 ice samples measured under a range of conditions relevant to the Uranus system, we determined that many of the spectral features between 4.8 and 5.25 μm can be attributed to collective oscillations across the crystalline lattice of thick CO_2 ice deposits (Figure 5). Furthermore, the multilobe scattering peaks expressed by the ν_3 mode of $^{12}CO_2$ on Ariel can be crudely approximated by a layer of CO_2 ice condensed on irradiated organic residues, as well as CO_2 deposited directly onto an Infragold substrate (Figure 6), highlighting the likely importance of surface roughness and grain boundaries for enhancing scattering. These same laboratory data can approximate the multilobe structure expressed by the ν_3 mode for $^{13}CO_2$ ice on Ariel and Umbriel (Figure 7), in particular when linearly mixed with a CO_2 clathrate spectrum (Figure 8)

presented in a prior study (A. Oancea et al. 2012). Laboratory spectra of CO_2 ice condensed on a meteorite simulant (amorphous $MgFeSiO_4$; T. Suhasaria et al. 2025) provide a less ideal match to the G395M data, but may contribute to Umbriel's broad $^{13}CO_2$ feature (Figure 9).

Notable exceptions to this story include the 4.02 μm band (Figure 10), which is difficult to explain with existing laboratory datasets of CO_2 ice, and instead, is better matched by carbonates, similar to Jupiter's moon Callisto (R. Johnson et al. 2004; R. J. Cartwright et al. 2024b). Our results also support the hypothesis that a 4.59 μm feature on Ariel and Umbriel could result from OCN^-, albeit a weak and poorly characterized shoulder feature seen in some laboratory data of CO_2 ice (G. B. Hansen 1997) may contribute to this band as well. To more fully understand the spectral properties of CO_2, CO, and other carbon oxides on Uranus' moons will require future laboratory experiments conducted under conditions relevant to the Uranian system, in particular for proper identification of species that express spectral features between 4.4 and 4.8 μm (Figure 2).

We explored whether CO_2 is dominated by radiolytic production mechanisms or internally derived components on Uranus' large moons, finding that the most likely outcome is a combination of both externally derived and internally sourced carbon oxides. The distributions of CO_2 and CO, concentrated on the trailing sides, primarily of the inner moons Ariel and Umbriel, would appear to be consistent with formation from charged particle bombardment, similar to the explanation for the distribution of CO_2 at the trailing hemisphere of Callisto (e.g., C. Hibbitts et al. 2000; R. J. Cartwright et al. 2024b). However, we found no trace of the common radiolytic product H_2O_2, whose production is enhanced when low levels of CO_2 are mixed with irradiated H_2O ice substrates (B. D. Mamo et al. 2025), suggesting that radiation processing may be of secondary importance at the orbits of Uranus' large moons. The potential presence of CO_2 clathrates and carbonates, perhaps supplied by geologic processes, also hints at the presence of internally derived carbon oxides on these moons. Furthermore, JWST has now detected CO_2 across the Uranian system, from its rings and ring moons to the irregular satellites (M. Belyakov & M. Brown 2024; M. Belyakov 2025), demonstrating the ubiquitous presence of this molecule and further confounding a simple "one size fits all" origin story.

Based on the steadily growing stockpile of spectral evidence collected by JWST, and other platforms over the past several decades, we postulate that a dual origin scenario is required to explain the presence of CO_2 on the large moons of Uranus. By analogy, a variety of studies have found evidence for both geologically exposed and radiolytically produced CO_2 on the Galilean satellites (e.g., T. McCord et al. 1998b; C. Hibbitts et al. 2002, 2003; R. J. Cartwright et al. 2024b, 2025), highlighting the different possible origins for this molecule on other icy moons. To fully explore the origin(s) of CO_2 and other carbon oxides will likely require data collected by a Uranus orbiter to assess the spatial relationships between CO_2-rich deposits and specific geologic features and terrains and to more precisely trace time-varying interactions between Uranus' magnetosphere and its rings and moons (National Academies of Sciences, Engineering, and Medicine 2023).

Acknowledgments

This work is based [in part] on observations made with the NASA/ESA/CSA James Webb Space Telescope. The data were obtained from the Mikulski Archive for Space Telescopes at the Space Telescope Science Institute, which is operated by the Association of Universities for Research in Astronomy, Inc., under NASA contract NAS 5-03127 for JWST. These observations are associated with GO program 1786. Support for GO program 1786 was provided by NASA through a grant from the Space Telescope Science Institute, which is operated by the Association of Universities for Research in Astronomy, Inc., under NASA contract NAS 5-03127. We thank O. Mivumbi, K. Guernon, C. Lantz, and L. Bouvet for help and support with INGMAR. INGMAR is a joint IAS-IJCLab facility funded by the P2IO LabEx (ANR-10-LABX-0038) in the framework Investissements d'Avenir (ANR-11-IDEX-0003-01). R.B. and S.C. acknowledge support from CNES (France) as part of their contributions to the JWST mission. E.Q. acknowledges financial support from the Centre National d'Études Spatiales (France) for the MAJIS/JUICE project. C.R.G. was supported by SwRI grant 15-R6440.

ORCID iDs

Richard J. Cartwright https://orcid.org/0000-0002-6886-6009
Sasha Cryan https://orcid.org/0009-0007-3966-1980
Rosario Brunetto https://orcid.org/0000-0003-3001-9362
Apolline Leclef https://orcid.org/0009-0008-0423-9525
Eric Quirico https://orcid.org/0000-0003-2768-0694
Bryan J. Holler https://orcid.org/0000-0002-6117-0164
William M. Grundy https://orcid.org/0000-0002-8296-6540
Tom A. Nordheim https://orcid.org/0000-0001-5888-4636
Ujjwal Raut https://orcid.org/0000-0002-6036-1575
Matthew M. Hedman https://orcid.org/0000-0002-8592-0812
Riley A. DeColibus https://orcid.org/0000-0002-1647-2358
Chloe B. Beddingfield https://orcid.org/0000-0001-5048-6254
Marc Neveu https://orcid.org/0000-0002-6220-2869
Christopher R. Glein https://orcid.org/0000-0002-2161-4672
Sara Faggi https://orcid.org/0000-0003-0194-5615
Geronimo L. Villanueva https://orcid.org/0000-0002-2662-5776
Noemi Pinilla-Alonso https://orcid.org/0000-0002-2770-7896
Stephanie M. Menten https://orcid.org/0000-0002-2430-0185

References

Afanasiev, V., Rosenbush, V., & Kiselev, N. 2014, AstBu, 69, 211
Aoki, S., Sato, Y., Giuranna, M., et al. 2018, Icar, 302, 175
Bauer, J. M., Roush, T. L., Geballe, T. R., et al. 2002, Icar, 158, 178
Becker, T., Zolotov, M., Gudipati, M., et al. 2024, SSRv, 220, 49
Beddingfield, C., Burr, D., & Emery, J. 2015, Icar, 247, 35
Beddingfield, C. B., & Cartwright, R. J. 2021, Icar, 367, 114583
Beddingfield, C. B., Cartwright, R. J., Jozwiak, L. M., Nordheim, T. A., & Patterson, G. W. 2025, PSJ, 6, 32
Beddingfield, C. B., Cartwright, R. J., Leonard, E., Nordheim, T., & Scipioni, F. 2022a, PSJ, 3, 106

Beddingfield, C. B., Leonard, E., Cartwright, R. J., Elder, C., & Nordheim, T. A. 2022b, PSJ, 3, 174
Beddingfield, C. B., Leonard, E. J., Nordheim, T. A., Cartwright, R. J., & Castillo-Rogez, J. C. 2023, PSJ, 4, 211
Bell, J. F., Calvin, W. M., Ockert-Bell, M. E., et al. 1996, JGR, 101, 9227
Belyakov, M. 2025, Ice Giant System Seminar Series, https://icegiants.jhuapl.edu/Events-and-Updates/Agenda/index.php?id=35
Belyakov, M., & Brown, M. 2024, AAS/DPS Meeting, 56, 405.02
Bennett, C., Jones, B., Knox, E., et al. 2010a, ApJ, 723, 641
Bennett, C. J., Jamieson, C. S., & Kaiser, R. I. 2010b, PCCP, 12, 4032
Bernstein, M. P., Sandford, S. A., & Allamandola, L. J. 1997, ApJ, 476, 932
Bertie, J. t., & Whalley, E. 1964, JChPh, 40, 1637
Bini, R., Salvi, P., Schettino, V., & Jodl, H.-J. 1991, PhLA, 157, 273
Bishop, J., King, S., Lane, M., et al. 2021, E&SS, 8, e2021EA001844
Bland, M. T., Beddingfield, C. B., Nordheim, T. A., Patthoff, D. A., & Vance, S. D. 2023, Icar, 395, 115452
Bohlin, R. C., & Landolt, A. U. 2015, AJ, 149, 122
Böker, T., Beck, T., Birkmann, S., et al. 2023, PASP, 135, 038001
Boogert, A., Brewer, K., Brittain, A., & Emerson, K. 2022, ApJ, 941, 32
Brown, M. E., Trumbo, S. K., Davis, M. R., & Chandra, S. 2025, PSJ, 6, 229
Brunetto, R., Hénault, E., Cryan, S., et al. 2025, ApJL, 982, L8
Brunken, N. G., Rocha, W. R., Van Dishoeck, E. F., et al. 2024, A&A, 685, A27
Buratti, B. J., & Mosher, J. A. 1991, Icar, 90, 1
Bushouse, H., Eisenhamer, J., Dencheva, N., et al. 2023, JWST Calibration Pipeline, v1.11.0, Zenodo, doi:10.5281/zenodo.8067394
Calvin, W. M., Johnson, R. E., & Spencer, J. R. 1996, GeoRL, 23, 673
Carlson, R., Anderson, M., Johnson, R., et al. 1999, Sci, 283, 2062
Carrozzo, F. G., De Sanctis, M. C., Raponi, A., et al. 2018, SciA, 4, e1701645
Cartwright, R., Beddingfield, C., Nordheim, T., et al. 2021, PSJ, 2, 120
Cartwright, R. J., DeColibus, R. A., Castillo-Rogez, J. C., et al. 2023, PSJ, 4, 42
Cartwright, R. J., Emery, J. P., Grundy, W. M., et al. 2020a, Icar, 338, 113513
Cartwright, R. J., Emery, J. P., Pinilla-Alonso, N., et al. 2018, Icar, 314, 210
Cartwright, R. J., Emery, J. P., Rivkin, A. S., Trilling, D. E., & Pinilla-Alonso, N. 2015, Icar, 257, 428
Cartwright, R. J., Nordheim, T. A., Cruikshank, D. P., et al. 2020b, ApJL, 902, L38
Cartwright, R. J., Beddingfield, C. B., Nordheim, T. A., et al. 2020c, ApJL, 898, L22
Cartwright, R. J., Nordheim, T. A., DeColibus, R. A., et al. 2022, PSJ, 3, 8
Cartwright, R. J., Holler, B. J., Grundy, W. M., et al. 2024a, ApJL, 970, L29
Cartwright, R. J., Villanueva, G. L., Holler, B. J., et al. 2024b, PSJ, 5, 60
Cartwright, R. J., Hibbitts, C. A., Holler, B. J., et al. 2025, PSJ, 6, 125
Chen, Y.-J., Nuevo, M., Chu, C.-C., et al. 2011, AdSpR, 47, 1633
Clark, R. N., Brown, R. H., Cruikshank, D. P., & Swayze, G. A. 2019, Icar, 321, 791
Clark, R. N., Curchin, J. M., Hoefen, T. M., & Swayze, G. A. 2009, JGRE, 114, E03001
Cohen, I. J., Turner, D. L., Kollmann, P., et al. 2023, GeoRL, 50, 8 e2022GL101998
Cooke, I. R., Fayolle, E. C., & Öberg, K. I. 2016, ApJ, 832, 5
Cruikshank, D. P., Roush, T. L., Owen, T. C., et al. 1993, Sci, 261, 742
Cryan, S., Brunetto, R., Guilbert-Lepoutre, A., et al. 2025, ApJ, 993, 188
Dartois, E. 2011, Icar, 212, 950
Dartois, E., Deboffle, D., & Bouzit, M. 2010, A&A, 514, A49
Dartois, E., & Schmitt, B. 2009, A&A, 504, 869
De Prá, M. N., Hénault, E., Pinilla-Alonso, N., et al. 2025, NatAs, 9, 252
De Sanctis, M. C., Ammannito, E., Raponi, A., et al. 2015, Natur, 528, 241
De Sanctis, M. C., Raponi, A., Ammannito, E., et al. 2016, Natur, 536, 54
DeColibus, R. A., Cartwright, R. J., Grundy, W. M., et al. 2026, PSJ, 7, 67
DeColibus, R. A., Chanover, N. J., & Cartwright, R. J. 2022, PSJ, 3, 119
DeColibus, R. A., Chanover, N. J., & Cartwright, R. J. 2023, PSJ, 4, 191
Denton, C., Scully, J., Castillo-Rogez, J., et al. 2026, JGRE, 131, e2025JE009282
DiLella, D., & Tevault, D. 1986, CPL, 126, 38
Dows, D. A., & Schettino, V. 1973, JChPh, 58, 5009
Escribano, R. M., Muñoz Caro, G. M., Cruz-Diaz, G. A., Rodríguez-Lazcano, Y., & Maté, B. 2013, PNAS, 110, 12899
Ewing, G. E., & Pimentel, G. C. 1961, JChPh, 35, 925
Fink, U., & Sill, G. T. 1982, The Infrared Spectral Properties of Frozen Volatiles (Univ. Arizona Press)
Fray, N., & Schmitt, B. 2009, P&SS, 57, 2053
Gerakines, P., & Moore, M. 2001, Icar, 154, 372
Gerakines, P., Moore, M. H., & Hudson, R. L. 2000, A&A, 357, 793
Gerakines, P. A., Bray, J., Davis, A., & Richey, C. 2005, ApJ, 620, 1140
Gerakines, P. A., & Hudson, R. L. 2020, ApJ, 901, 52
Gerakines, P. A., Materese, C. K., & Hudson, R. L. 2023, MNRAS, 522, 3145
Gerakines, P. A., Yarnall, Y. Y., & Hudson, R. L. 2022, MNRAS, 509, 3515
Ghosh, J., Vishwakarma, G., Kumar, R., & Pradeep, T. 2023, Accounts of Chemical Research, 56, 2241
Glein, C. R., & Waite, J. H. 2020, GeoRL, 47, e2019GL085885
Gomis, O., & Strazzulla, G. 2005, Icar, 177, 570
Gourgeot, F., Dumas, C., Merlin, F., Vernazza, P., & Alvarez-Candal, A. 2014, A&A, 562, A46
Grim, R. J., & Greenberg, J. M. 1987, ApJ, 321, L91
Grundy, W., Schmitt, B., & Quirico, E. 2002, Icar, 155, 486
Grundy, W., Young, L., Spencer, J., et al. 2006, Icar, 184, 543
Grundy, W., Young, L., Stansberry, J., et al. 2010, Icar, 205, 594
Grundy, W., Young, L., & Young, E. 2003, Icar, 162, 222
Hage, W., Liedl, K. R., Hallbrucker, A., & Mayer, E. 1998, Sci, 279, 1332
Hanel, R., Conrath, B., Flasar, F., et al. 1986, Sci, 233, 70
Hansen, G. B. 1997, AdSpR, 20, 1613
Hapke, B. 2012, Theory of Reflectance and Emittance Spectroscopy (Cambridge Univ. Press)
Hedman, M., Tiscareno, M., Showalter, M., et al. 2024, JGRE, 129, e2023JE008236
Helfenstein, P., Hillier, J., Weitz, C., & Veverka, J. 1991, Icar, 90, 14
Helfenstein, P., Thomas, P. C., & Veverka, J. 1989, Natur, 338, 324
Hénault, E., Brunetto, R., Pinilla-Alonso, N., et al. 2025, A&A, 694, A126
Hendrix, A. R., Filacchione, G., Paranicas, C., Schenk, P., & Scipioni, F. 2018, Icar, 300, 103
Herr, K. C., & Pimentel, G. C. 1970, Sci, 167, 47
Hexter, R. 1958, AcSpe, 10, 281
Hibbitts, C., Klemaszewski, J., McCord, T., Hansen, G., & Greeley, R. 2002, JGRE, 107, 5084
Hibbitts, C., McCord, T., & Hansen, G. 2000, JGR, 105, 22541
Hibbitts, C., Pappalardo, R., Hansen, G., & McCord, T. 2003, JGRE, 108, 5036
Holler, B., Young, L., Grundy, W., & Olkin, C. 2016, Icar, 267, 255
Hudson, R., Moore, M., & Gerakines, P. 2001, ApJ, 550, 1140
Jacox, M. E., Milligan, D. E., Moll, N. G., & Thompson, W. E. 1965, JChPh, 43, 3734
Jakobsen, P., Ferruit, P., de Oliveira, C. A., et al. 2022, A&A, 661, A80
Johnson, R., Carlson, R., Cooper, J., et al. 2004, Jupiter: The Planet, Satellites and Magnetosphere (Cambridge Univ. Press), 485
Johnson, R., & Jesser, W. 1997, ApJL, 480, L79
Kazakov, K., & Vigasin, A. 2021, MolPh, 119, e1934581
Loeffler, M., Baratta, G., Palumbo, M., Strazzulla, G., & Baragiola, R. 2005, A&A, 435, 587
Mamo, B. D., Raut, U., Teolis, B. D., et al. 2025, PSJ, 6, 170
Mangan, T., Salzmann, C., Plane, J., & Murray, B. 2017, Icar, 294, 201
Markwardt, L., Wen Lin, H., Holler, B. J., et al. 2025, PSJ, 6, 154
Mastrapa, R., Sandford, S., Roush, T., Cruikshank, D., & Dalle Ore, C. 2009, ApJ, 701, 1347
McClure, M. K., Rocha, W., Pontoppidan, K., et al. 2023, NatAs, 7, 431
McCord, T., Hansen, G., Fanale, F., et al. 1998a, Sci, 280, 1242
McCord, T., Carlson, R., Smythe, W., et al. 1997, Sci, 278, 271
McCord, T., Hansen, G., Clark, R., et al. 1998b, JGRE, 103, 8603
Menten, S. M., Sori, M. M., Bramson, A. M., Nordheim, T. A., & Cartwright, R. J. 2024, JGRE, 129, e2024JE008376
Moll, N. G., Clutter, D. R., & Thompson, W. E. 1966, JChPh, 45, 4469
Montmessin, F., Gondet, B., Bibring, J.-P., et al. 2007, JGRE, 112, E11S90
Moore, M., & Khanna, R. 1991, AcSpA, 47, 255
Mousis, O., Lunine, J. I., Thomas, C., et al. 2009, ApJ, 691, 1780
National Academies of Sciences, Engineering, and Medicine 2023, Origins, Worlds, and Life: A Decadal Strategy for Planetary Science and Astrobiology 2023-2032 (The National Academies Press)
Nyquist, R. A., Leugers, M. A., & Putzig, C. L. 1997, The handbook of infrared and raman spectra of inorganic compounds and organic salts: a 4-volume set (Academic)
Oancea, A., Grasset, O., Le Menn, E., et al. 2012, Icar, 221, 900
Oza, A. V., Johnson, R. E., Schmidt, C. A., & Calvin, W. M. 2026, AsBio, 26, 472
Pendleton, Y., Tielens, A., Tokunaga, A., & Bernstein, M. 1999, ApJ, 513, 294
Peterson, G., Nimmo, F., & Schenk, P. 2015, Icar, 250, 116
Potapov, A., Linz, H., Bouwman, J., et al. 2025, A&A, 697, A53
Protopapa, S., Raut, U., Wong, I., et al. 2024, NatCo, 15, 8247

Quirico, E., & Schmitt, B. 1997a, Near-IR optical constants of crystalline CO2 ice at 179K completed with 28K data, SSHADE, doi:10.26302/SSHADE/EXPERIMENT_BS_20130215_001
Quirico, E., & Schmitt, B. 1997b, Icar, 127, 354
Raunier, S., Chiavassa, T., Allouche, A., Marinelli, F., & Aycard, J.-P. 2003, CP, 288, 197
Rauscher, B. J. 2024, PASP, 136, 015001
Raut, U., & Baragiola, R. 2013, ApJ, 772, 53
Raut, U., Fulvio, D., Loeffler, M., & Baragiola, R. 2012, ApJ, 752, 159
Raut, U., Peterson, T., Mamo, B. D., et al. 2025, EPSC-DPS Joint Meeting, 2025, 393
Rayner, J. T., Toomey, D., Onaka, P., et al. 2003, PASP, 115, 362
Sandford, S., Allamandola, L., Tielens, A., & Valero, G. 1988, ApJ, 329, 498
Schenk, P. M. 1991, JGRB, 96, 1887
Scully, J. E., Denton, C. A., Castillo-Rogez, J. C., et al. 2025, PSJ, 6, 187
Sharkey, B. N., Rivkin, A. S., Cartwright, R. J., et al. 2025, PSJ, 6, 242
Smith, B. A., Soderblom, L., Beebe, R., et al. 1986, Sci, 233, 43
Sori, M. M., Bapst, J., Bramson, A. M., Byrne, S., & Landis, M. E. 2017, Icar, 290, 1
Soto, C., Holler, B., & Cartwright, R. 2025, AAS Meeting, 246, 202.01
Souza-Feliciano, A., Holler, B., Pinilla-Alonso, N., et al. 2024, A&A, 681, L17
Spencer, J. R., & Calvin, W. M. 2002, AJ, 124, 3400
Steckloff, J. K., Goldstein, D., Trafton, L., Varghese, P., & Prem, P. 2022, Icar, 384, 115092
Strazzulla, G., Brucato, J., Palumbo, M., & Spinella, F. 2007, MmSAI, 78, 681
Sturm, J., McClure, M., Bergner, J., et al. 2023, A&A, 677, A18
Suhasaria, T., Leuschner, V., Jaeger, C., Gieser, C., & Henning, T. 2025, ApJL, 988, L27
Taylor, J. 1997, Introduction to Error Analysis, The Study of Uncertainties in Physical Measurements (MIT Press)
Tegler, S., Cartwright, R., Grundy, W., et al. 2026, PSJ, 7, 191
Trumbo, S. K., & Brown, M. E. 2023, Sci, 381, 1308
Trumbo, S. K., Brown, M. E., Bockelée-Morvan, D., et al. 2023, SciA, 9, eadg3724
Van Broekhuizen, F., Keane, J., & Schutte, W. 2004, A&A, 415, 425
Villanueva, G., Hammel, H., Milam, S., et al. 2023, Sci, 381, 1305
Vyjidak, A., Giuliano, B. M., Jusko, P., et al. 2026, A&A, 707, A214
Whalley, E. 1977, CaJCh, 55, 3429
Wong, I., Holler, B., Protopapa, S., et al. 2025, LPICo, 3059, 7047